Check for updates

Water Resources Research

RESEARCH ARTICLE
10.1029/2024WR038391

Causal Discovery Analysis Reveals Global Sources of Predictability for Regional Flash Droughts

Sudhanshu Kumar[1] **and Di Tian**[1]

[1]Department of Crop, Soil & Environmental Sciences, Auburn University, Auburn, AL, USA

Key Points:

- Causal discovery framework identified local and remote regions over the globe causing U.S. Flash droughts (FDs)
- Machine learning with climate variables over the discovered regions can well predict U.S. FDs up to 4 weeks in advance
- The discovered regions are consistent with the known sources of predictability but also reveal potentially new sources of predictability

Supporting Information:

Supporting Information may be found in the online version of this article.

Correspondence to:

D. Tian,
tiandi@auburn.edu

Citation:

Kumar, S., & Tian, D. (2024). Causal discovery analysis reveals global sources of predictability for regional flash droughts. *Water Resources Research*, *60*, e2024WR038391. https://doi.org/10.1029/2024WR038391

Received 10 JUL 2024
Accepted 10 NOV 2024

Author Contributions:

Conceptualization: Sudhanshu Kumar, Di Tian
Data curation: Sudhanshu Kumar
Formal analysis: Sudhanshu Kumar, Di Tian
Funding acquisition: Di Tian
Investigation: Sudhanshu Kumar, Di Tian
Methodology: Sudhanshu Kumar, Di Tian
Project administration: Di Tian
Resources: Di Tian
Software: Sudhanshu Kumar, Di Tian
Supervision: Di Tian
Validation: Sudhanshu Kumar, Di Tian
Visualization: Sudhanshu Kumar
Writing – original draft: Sudhanshu Kumar

© 2024. The Author(s).
This is an open access article under the terms of the Creative Commons Attribution-NonCommercial-NoDerivs License, which permits use and distribution in any medium, provided the original work is properly cited, the use is non-commercial and no modifications or adaptations are made.

Abstract Detecting and quantifying the global teleconnections with flash droughts (FDs) and understanding their causal relationships is crucial to improve their predictability. This study employs causal effect networks (CENs) to explore the global predictability sources of subseasonal soil moisture FDs in three regions of the United States (US): upper Mississippi, South Atlantic Gulf (SAG), and upper and lower Colorado river basins. We analyzed the causal relationships of FD events with global 2-m air temperature, sea surface temperature, water deficit (precipitation minus evaporation), and geopotential height at 500 hPa at the weekly timescale over the warm season (April to September) from 1982 to 2018. CENs revealed that the Indian Ocean Dipole, Pacific North Atlantic patterns, Bermuda high-pressure system, and teleconnection patterns via Rossby wave train and jet streams strongly influence FDs in these regions. Moreover, a strong link from South America suggests that atmospheric circulation forcings could affect the SAG through the low-level atmospheric flow, reducing inland moisture transport, and leading to a precipitation deficit. Machine learning utilizing the identified causal regions and factors can well predict major FD events up to 4 weeks in advance, providing useful insights for improved subseasonal forecasting and early warnings.

Plain Language Summary This study investigates the global factors affecting flash droughts (FDs) in the upper Mississippi, South Atlantic Gulf, and upper and lower Colorado river basins in the United States. Using causal effect networks, the research identifies key global influences, such as the Indian Ocean Dipole, Pacific North Atlantic patterns, and Bermuda high-pressure system, which affect FDs through atmospheric circulation and jet streams. Findings show that these factors, along with local and remote climate processes, can predict FDs up to 4 weeks in advance. Machine learning models utilizing these climate variables effectively forecast FDs events. The study highlights the importance of large-scale climate oscillations and teleconnections in predicting FDs, offering useful insights for improving early warnings and climate risk management.

1. Introduction

Over the past few decades, increasing drought events have been observed around the globe, causing severe effects (Chiang et al., 2021), from energy shortages to significant food and water insecurity. Under global warming, the intensity and frequency of droughts are predicted to increase in the upcoming decades and will have deleterious impacts on natural resources, crop production, and the environment (Seneviratne et al., 2012). The increasing drought poses an increased risk for wildfire and heatwave development, depletion of water resources, reduction of air quality, and threatened food security (Christian et al., 2020; Hoell et al., 2020; Otkin et al., 2019; Yuan et al., 2019).

Droughts typically occur at larger spatiotemporal scales (Konapala & Mishra, 2017), spread over hundreds of kilometers and often lasting for weeks to months and years (Konapala & Mishra, 2017; Mishra & Singh, 2010). However, the absence of precipitation events during the growing season, combined with high temperatures and abundant sunshine, led to rapid decreases in soil moisture (SM) content and the rapid emergence of flash drought (FD) conditions (Mo & Lettenmaier, 2015; Otkin et al., 2013). FDs, as an extreme hydro-climate event at the subseasonal (weeks to months) timescale, are still challenging to understand and predict (Hoerling et al., 2014), due to their rapid onset and development and complex processes and phenomena that contribute to or affect their onset and development (DeAngelis et al., 2020; Hoell et al., 2020; Mo & Lettenmaier, 2020; Pendergrass et al., 2020). These FDs can cause a dramatic increase in water stress and even crop failure in a few weeks (Hoffmann et al., 2021; USDA, 2017). The 2012 U.S. FD exemplifies this phenomenon, where drought coverage and intensity rapidly increased during June and July due to anomalous weather conditions, resulting in nearly 80%

Writing – review & editing: Di Tian

of the contiguous U.S. being characterized by at least abnormally dry conditions by the end of summer, according to the U.S. Drought Monitor (USDM; Svoboda et al., 2002).

Studies have been performed extensively to understand FDs over the past few years. Hoerling et al. (2014) found that the proximate cause of the 2012 Great Plains FD was due to a reduction in atmospheric moisture transport from the Gulf of Mexico to the Great Plains, resulting from natural variations in atmospheric circulation anomalies. Extreme heatwave conditions and precipitation deficits over the Great Plains in 2012 were associated with an arid atmosphere and led to rapid additional soil drying. Another study, which looked at the prior meteorological conditions of FDs during 1979 and 2010, discovered that FDs over the eastern United States (US) were likely driven by atmospheric ridging in the mid to upper level troposphere (Ford & Labosier, 2017), which was part of a quasi-stationary Rossby wave train (Ambrizzi et al., 1995). Recently, based on numerical modeling experiments, Schubert et al. (2021) showed the impact of the Indian Ocean Dipole (IOD), an irregular oscillation of sea surface temperature (SST), on the 2019 southeastern US FD. Long-term statistical analysis has revealed that SST over a region of the Pacific Ocean had strong influences on heatwaves from 1950 to 2015 in the US (McKinnon et al., 2016), the events often compounded with FDs (Miralles et al., 2019; Mo & Lettenmaier, 2015). Since SST in the Indian, Pacific, and Atlantic oceans were found to be connected with Rossby wave trains (Lim, 2015; McIntosh & Hendon, 2018), a large-scale circulation phenomenon associated with FDs (DeAngelis et al., 2020; Ford & Labosier, 2017; Wang et al., 2014), SST in Indian, Pacific, and Atlantic oceans will likely cause FDs over different regions; and increase in surface temperatures at landmasses nearby these oceans are directly linked with SM deficits (Christian et al., 2020; Manthos et al., 2022). Additionally, lower evapotranspiration due to SM deficits reduces atmospheric moisture, further increasing atmospheric evaporative demand and exacerbating SM depletion (Teuling et al., 2013). Yin et al. (2023) suggest that the precipitation shortage and the vapor pressure deficit increase also cause the occurrence of FDs. However, these previous studies only focused on analyzing either temperature impacts on a single FD event or local impacts from mesoscale meteorological conditions. The long-term causal relationships of subseasonal FDs with temperature, pressure, and water deficit (WD) (precipitation minus evaporation) from different regions of the globe have not yet been systematically investigated.

Studies explored proximate causes of FDs based on simple correlation and regression or sophisticated numerical modeling experiments (Ford & Labosier, 2017; Schubert et al., 2021; Wang et al., 2014). Ford and Labosier (2017) used logistic regression to account for variables linked with the likelihood of FD occurrence. Mahto and Mishra (2023) used the Pearson's Correlation Coefficient to estimate the relationship between two variables and dominance analysis to evaluate the percentage contribution of precipitation and vapor pressure deficit in FD occurrence. Correlation and regression approaches are affected by autocorrelation effects, indirect connections via a third process, or a typical driver leading to noncausal, spurious correlations that limit interpretability (Runge, Nowack, et al., 2019). Additionally, numerical modeling experiments are limited by the physical realism of the model, which experiences difficulties in capturing important processes, such as land-atmosphere feedback (Miralles et al., 2019), land surface water and energy budgets (Tian et al., 2016, 2018), moisture transport (Roy et al., 2019), and Rossby wave propagation (Gray et al., 2014) due to model resolutions and biases. Such limitations can affect modeling performance for analyzing the causes of the 2019 southeastern U.S. FD (Schubert et al., 2021). As a result, the accuracy and predictive capabilities of the current S2S models' forecasts are still limited, with the predictive skill for FD events often lower than that of climatology for forecasts extending beyond 2 weeks (Lesinger et al., 2024; Ma & Yuan, 2023; Su et al., 2023). Research by Ma and Yuan (2023) showed that only 20% of FD events could be accurately predicted 1 week in advance in China, but this accuracy dropped to 4% by the third week, highlighting the significant challenges in predicting FDs at the subseasonal scale. Lorenz et al. (2021) evaluated week 3–4 changes in Root-Zone Soil Moisture (RZSM), which is a FD indicator, and identified low skill due in part to autocorrelation.

Pendergrass et al. (2020) noted that the development of FD events is influenced by a variety of global and regional factors, including land-atmosphere interactions, the Madden-Julian Oscillation (MJO), and the IOD. Discovering and harnessing existing and new sources of predictability over the globe can be potentially useful for improving regional FD predictions. Causal inference analysis based on long-term observational data has the potential to discover underlying drivers and predictability sources of FDs. It can overcome spurious correlations due to autocorrelation, indirect effects, or common drivers, and discover the complex interactions among different driving factors and the variable of interest (Kretschmer et al., 2017; Kumar et al., 2023; Runge, Nowack, et al., 2019). With growing volume and quality of observational-based climate data being available, causal

19447973, 2024, 11, Downloaded from https://agupubs.onlinelibrary.wiley.com/doi/10.1029/2024WR038391 by Auburn University Libraries, Wiley Online Library on [24/02/2025]. See the Terms and Conditions (https://onlinelibrary.wiley.com/terms-and-conditions) on Wiley Online Library for rules of use; OA articles are governed by the applicable Creative Commons License

19447973, 2024, 11, Downloaded from https://agupubs.onlinelibrary.wiley.com/doi/10.1029/2024WR038391 by Auburn University Libraries, Wiley Online Library on [24/02/2025]. See the Terms and Conditions (https://onlinelibrary.wiley.com/terms-and-conditions) on Wiley Online Library for rules of use; OA articles are governed by the applicable Creative Commons License

inference approach can provide a great opportunity to disentangle the complex effects of both local and remote drivers of FDs and discover their sources of predictability by directly learning from observations.

In summary, the causal relationships between FDs and their potential global drivers are still not well understood, and current dynamic models show limited predictive capabilities beyond 2 weeks. In this study, we attempt to address these research gaps by exploring global sources of predictability of SM FDs using causal inference framework. We quantified the causal relationships of regional FDs in the U.S. with 2-m air temperature, SST, geopotential height at 500 hPa, and WD over the quasi-globe. The analysis revealed local and remote sources of predictability, which, combined with machine learning, well predicted FD events up to 4 weeks in advance. Moreover, we discussed plausible mechanisms related to the identified sources of predictability. The findings of this study may be helpful for improving FD predictability and early warnings.

2. Methods

2.1. Data and Potential Drivers

The Root-Zone Soil Moisture (RZSM) was obtained from a multi-decadal SMERGEv2.0 product developed by merging satellite retrievals from the European Space Agency Climate Change Initiative (ESA-CCI) SM and model output from the North American Land Data Assimilation System (NLDAS; Crow & Tobin, 2018), which significantly enhances its accuracy and relevance for long- and short-term climate analysis. The data set has been validated and compared with other satellite and in situ observations (Tobin et al., 2019, 2021) and has been found to be a reliable data set for agricultural drought applications (Tobin et al., 2019). This product has been used in several previous research relating SM and FD (Corak et al., 2024; Lorenz et al., 2021; Osman et al., 2022; Shin et al., 2023). Hence, for this study, daily RZSM data with rooting depth up to 40 cm and a spatial resolution of 0.125° over the entire continental US (CONUS) was used from January 1982 to December 2018. SM at 40 cm closely aligns with the active root zone for crops, directly impacting agricultural productivity and water management. This depth offers the most relevant data for assessing crop health, whereas shallower or deeper measurements may be less representative of plant-available water (de Moraes et al., 2023; Fan et al., 2016; Liu et al., 2023).

MERRA-2 is the climate reanalysis developed by the National Aeronautics and Space Administration (NASA), which uses the latest V5 Global Modeling and Assimilation Office (GMAO) (GOES) data assimilation with an updated grid-to-point statistical interpolation (Gelaro et al., 2017) and has a horizontal resolution of $0.5° \times 0.625°$. Gelaro et al. (2017) presents the underlying alterations implemented in the reanalysis framework for MERRA-2, which set it apart from its predecessor, MERRA. This study used the Geopotential height at 500 hPa (Z500; GMAO, 2015a), 2m air temperature (T2m), sea level pressure, eastward wind at 850 hPa, northward wind at 850 hPa (GMAO, 2015c), surface latent heat flux and bias-corrected total precipitation (GMAO, 2015b). More details are available in the published MERRA-2 data product file (Bosilovich et al., 2015).

All data sets have been obtained for a common period from 01 Jan 1982, to 31 Dec 2018, and have been bilinearly interpolated to a consistent $1° \times 1°$ grid. Evaporation is converted from latent heat flux by dividing latent heat of vapourization (λ), where: $\lambda = 2.501 - (2.361 \times 10^{-3}) \times$ T2m. Finally, we calculated weekly WD using the MERRA2 precipitation and evaporation (precipitation-evaporation, P-E). Since this research focuses on the subseasonal variability, we removed the centered 120-day moving average for each variable at each grid point (Arcodia et al., 2020; Malloy & Kirtman, 2023). We perform the analysis only for the warm season (April to September) given the occurrences and impacts of FD events during the warm period (Koster et al., 2019; Lesinger & Tian, 2022). All variables were aggregated into weekly, a timescale commonly considered for monitoring FDs (Pendergrass et al., 2020).

2.2. FD and Study Region

For this work, we used RZSM percentile to quantify agricultural drought, while a specific criterion will be used to define "flash." Previous studies noted that although the principle of rapid intensification of drought conditions has been widely adopted in FD definitions, currently there is not a universally accepted definition or criteria for FD (Lisonbee et al., 2022; Osman et al., 2021). Since this research focuses on agricultural FDs, our FD definition is based on SM given its direct influence on plant productivity and water use (e.g., Novick et al., 2016; Rigden et al., 2020). For detecting a FD event, the SM percentile drop (SMPD) was used, which is one of the most

representative SM-based definitions (e.g., Osman et al., 2021; Yuan et al., 2019). Specifically, FD occurs when the 1-week running average SM falls from the 40th to the twentieth percentile in less than or equal to four weeks. Osman et al. (2021) concluded that the RZSM shows the clearest signal when FDs occur. After FD event identification, each grid point over the region is binarized depending on whether it was under FD or not and was assigned 1 (occur) or 0 (not occur) (Zhou et al., 2020). To obtain a single quantity representative of the occurrence and spatial extent of weekly SM FD from 1982 to 2018, we calculated the area under FD over each study region for each week, referred as FD percentage coverage (FD-pc). FD-pc is a single quantity representative of both the occurrence and spatial extent of FDs for each week during the study period. Various definitions of FD have been applied across different contexts to detect its occurrence (Tyagi et al., 2022). However, those definitions often lead to underestimation or overestimation of the frequency of occurrence and spatial extent of FD (Hoffmann et al., 2021; Mo & Lettenmaier, 2020; Zhang et al., 2017). In our study, both the occurrence and coverage of FD are critical factors.

We selected the three study regions of the US— South Atlantic-Gulf (SAG), upper Mississippi (UM), and upper and lower Colorado (ULC) river basins—using the US Geological Survey- Hydrologic Unit Code (USGS HUC02) on NCA-LDAS grid and are marked as A, B, and C respectively in Figure 1a. The SAG in the southeast has experienced more frequent FD events than the other regions over the past decades (Lesinger & Tian, 2022; Mo & Lettenmaier, 2016). Projected increase in warming in the upcoming decades can increase the frequency of FDs in the SAG (Mahto & Mishra, 2023). This region has already been experiencing increased irrigation demand due to rising climate pressures during the past decades (USDA, 2017) and has strong teleconnections with large-scale climate patterns (Hansen et al., 1998). The major land use in the UM basin is cropland dominated by corn and soybean (USDA, 2014). These agricultural areas witnessed many droughts in the last decades. The ULC river basin in the southwest is one of the most over-allocated basins of the world, providing water to 40 million people in Colorado and downstream states. However, temperature rise, and extended droughts have been observed since 2000 due to anthropogenic climate change, and the future of the ULC river basin is looming (Hung et al., 2022; Tran et al., 2022). Analyzing FD causal factors and teleconnections of these basins can help understand FD predictability and improve FD assessment and early warning. Moreover, these three regions were chosen for this study to demonstrate the replicability of the model across different locations with diverse SM and climate patterns. By selecting regions with varying environmental conditions, we aim to validate that the model can be effectively applied in any region, showcasing its versatility and robustness.

2.3. Causal Discovery Framework

We use causal discovery framework to detect and visualize the causal relationships from reanalysis/observational-based data. Causal discovery aims to uncover the underlying causal structure that explains how variables influence each other. It moves beyond mere associations to understand the mechanisms and interventions that can reveal the effects of changes in one variable on another, which is crucial for understanding and predicting global spatial and temporal teleconnections of U.S. FDs. The causal discovery framework includes causal effect network (CEN) and causal inference analysis, as described below.

2.3.1. Causal Effect Network (CEN)

(CEN) analysis goes beyond merely identifying connections between variables, as seen in causal networks, by pinpointing how changes in one variable can cause changes in another. This distinction between correlation, which shows variables moving together without implying a direct influence, and causation, where one variable's alteration directly affects another, is crucial. Causation demands stronger evidence, often through experimental or longitudinal studies, to eliminate other potential influences. This analysis is especially useful for understanding complex causal relationships in climate science, such as the mechanisms leading to FDs, by mapping out the global causal links, their directions, and timings. The PCMCI algorithm is pivotal in CEN analysis for causal discovery in time series data, effectively handling high-dimensional data sets and identifying true causal relationships amidst indirect connections (Kretschmer et al., 2016; Runge, Nowack, et al., 2019). This methodology is foundational for interpreting CEN outcomes, enabling researchers to uncover underlying causal mechanisms in complex systems where direct experimentation may not be feasible, thus facilitating discoveries based on data insights.

19447973, 2024, 11, Downloaded from https://agupubs.onlinelibrary.wiley.com/doi/10.1029/2024WR038391 by Auburn University Libraries, Wiley Online Library on [24/02/2025]. See the Terms and Conditions (https://onlinelibrary.wiley.com/terms-and-conditions) on Wiley Online Library for rules of use; OA articles are governed by the applicable Creative Commons License

10.1029/2024WR038391

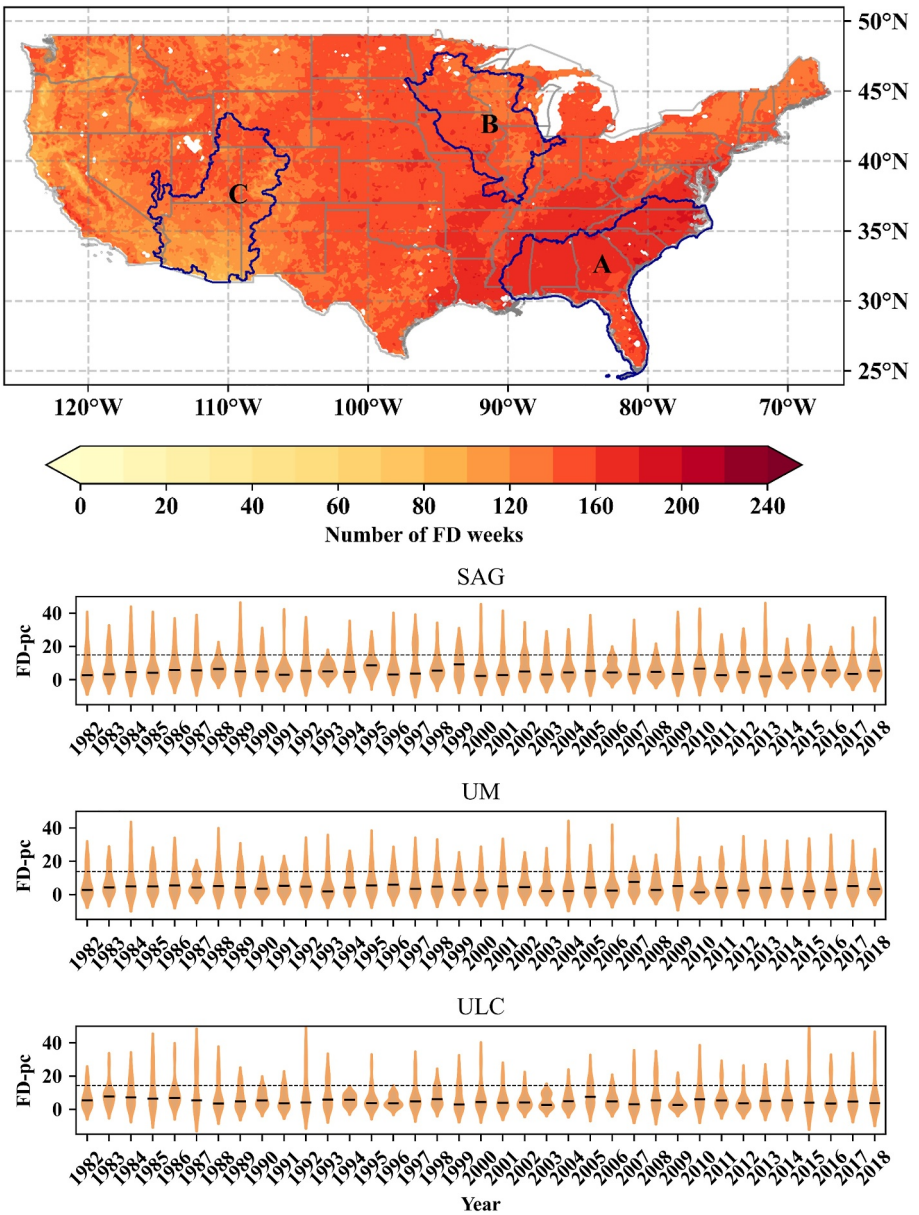

Figure 1. (a) Spatial variations of number of weeks under flash drought in United States in the warm period (1982–2018) with at least two events occurring concurrently. Regions A, B, and C represent the three study regions namely South Atlantic-Gulf, upper Mississippi, and upper & lower Colorado river basins respectively. (b) Yearly variation of FD-pc in the three study regions for the warm period. The median value for each distribution is shown with a black horizontal line, and the dashed line is at one standard deviation above the mean of FD-pc.

The PCMCI (Peter and Clark Momentary Conditional Independence) algorithm is efficient for detecting causal relationships between data sets (Runge, Bathiany, et al., 2019). It has advantages over existing approaches, such as Granger causality (Granger, 1969), in terms of detection power, which identifies the presence of causal relationships and quantifies their strength (Runge, Nowack, et al., 2019). This method combines the PC (Peter and Clark) technique (Spirtes & Glymour, 1991) and the momentary conditional independence (MCI) test.

The PC approach identifies a series of causal parents, considering both true positive and false positive linkages. In the PC step, the significance threshold (α) is selected to retain or discard a certain parent after calculating the partial correlation. This step involves first identifying the set P of n variables designated for analysis. The PC algorithm calculates direct correlations between the ith element (at zero lag) in set P and each of the remaining

19447973, 2024, 11, Downloaded from https://agupubs.onlinelibrary.wiley.com/doi/10.1029/2024WR038391 by Auburn University Libraries, Wiley Online Library on [24/02/2025]. See the Terms and Conditions (https://onlinelibrary.wiley.com/terms-and-conditions) on Wiley Online Library for rules of use; OA articles are governed by the applicable Creative Commons License

19447973, 2024, 11, Downloaded from https://agupubs.onlinelibrary.wiley.com/doi/10.1029/2024WR038391 by Auburn University Libraries, Wiley Online Library on [24/02/2025]. See the Terms and Conditions (https://onlinelibrary.wiley.com/terms-and-conditions) on Wiley Online Library for rules of use; OA articles are governed by the applicable Creative Commons License

elements in set P at a certain lag τ; the significant correlations form a set of potential parents X_i^0 at time lag τ, which is in increasing order of the correlation strength. Then, the algorithm calculates the partial correlation between the ith variable and each potential parent in the set X_i^0. This calculation was performed with the condition that the first variable in the set has the strongest correlation with this ith variable. The assessment aims to ascertain whether a common variable mediates the relationship between these variables. For instance, where three variables a, b, and c are in X, we calculate the partial correlation between a and b conditioned on c by performing a linear regression of a on c and b on c, followed by the correlation of the resultant residuals. If the partial correlation between a and b is still significant at a given confidence level α, a and b are conditionally dependent given variable c, that is, the correlation between a and b cannot be (exclusively) explained by the influence of variable c (not spurious link). This may reduce the set of parents for the next iteration X_i^0. The process is repeated for this set of parents but with now two conditions (and three in the next step), leading to a next (possibly reduced) set of parents X_i^0. The algorithm converges when the number of parents equals or exceeds the number of conditions needed to calculate the partial correlation. With a selected set of parents, the MCI test is then performed as the second step of the PCMCI algorithm.

The MCI test eliminates unnecessary conditions, even for data sets with high autocorrelation. The maximum time delay parameter ($\tau_{\max}$) is chosen to estimate time-lagged causal links (Runge, Nowack, et al., 2019). In the MCI step, we calculate the partial correlation between a variable and its parents at different time lags but are conditioned on the set of parents of the parents of the variable we are interested in. It removes common driver effects and reduces to a final set of causal parents. More details of this algorithm can be found in Runge, Nowack, et al. (2019).

Based on Causal Sufficiency, Faithfulness, and the Markov condition assumptions, the upgraded PCMCI+ method extends PCMCI by discovering full, lagged, and contemporaneous causal graphs. Contemporaneous link denotes a non-directional, simultaneous causal relationship between variables at the same time, challenging the causal precedence assumption. PCMCI+ has an additional orientation phase after the PC and MCI steps. The information of separating sets in MCI tests is used in the orientation phase, which results in a completed partially directed acyclic graph representing a Markov equivalence class. A Markov equivalence class contains all the causal graphs compatible with the data's conditional independence. PCMCI+ yields well-controlled false positives, higher recall, and optimized conditioning sets with substantially shorter runtimes than the original PC algorithm for autocorrelated time series (Runge, 2020). It flexibly combines nonlinear or linear conditional independence tests with a directed graphical causal model to estimate causal networks from time series data sets (Goswami et al., 2022).

To implement PCMCI+, the Tigramite v4.2 Python package (https://github.com/jakobrunge/tigramite) and the partial correlation conditional independence test were utilized (Kretschmer et al., 2018; Nowack et al., 2020; Runge, Nowack, et al., 2019). This study considered time-lagged linkages of up to 7 weeks, the maximum time delay for optimized results. The teleconnection indices were generated separately from the FD-pc time series to determine the causal relationships. The strength of causal links (climate variables → FD-pc) and their statistical significance ($p < 0.01$) were tracked, and, for the causation analysis at different lags, the strongest significant causal links and the associated week were recorded. For a detailed description of PCMCI+, the readers refer to the article by Runge (2020). Prior knowledge of physical systems and relevant variables with timescales is required for applying the PCMCI+ algorithm (Malloy & Kirtman, 2023; Runge, Nowack, et al., 2019); hence, we analyzed the causal maps of potential variables as described below.

2.3.2. Causal Inference Analysis

CEN is used in the causal inference analysis (Figure S4 in Supporting Information S1), which consists of three steps:

Step 1: Spatial causal maps for defining potential precursors from gridded climate variables.

To find potential global regions showing teleconnections with FD-pc, we investigate causal maps, which plot the linking coefficient from the causal effect network (CEN) spatially at each grid point over the quasi-globe (Di Capua et al., 2020). This step determines the causal link between a time series at each grid point for climate variables (weekly T2m, SST, Z500, or WD) and area-averaged one-dimensional time series (FD-pc). The analysis was performed on a weekly time scale with a statistical significance level of $p < 0.01$. The climate variables

19447973, 2024, 11, Downloaded from https://agupubs.onlinelibrary.wiley.com/doi/10.1029/2024WR038391 by Auburn University Libraries, Wiley Online Library on [24/02/2025]. See the Terms and Conditions (https://onlinelibrary.wiley.com/terms-and-conditions) on Wiley Online Library for rules of use; OA articles are governed by the applicable Creative Commons License

should have a lagged effect with FD-pc, as these variables influence the occurrence of FD events. Hence, this analysis was computed iteratively with a lag (τ) from 0 to 7 weeks, as the results do not change much after week 7. The strongest significant causal links were aggregated for each grid cell, and the spatial maps were generated. In this step, we also removed the links with a strength less than 0.05 as they are weak (Malloy & Kirtman, 2023) and do not influence the occurrence of FD much. Findings from these maps motivates us to test linkages from global T2m, Z500, and WD to regional FD-pc with a CEN and to confirm if the teleconnection from these global variables to regional FD-pc exists and the time lags for different connections.

Step 2: Clustering significant grid cells of climate variable driving FD from causal maps.

Grid cells with statistically significant higher strength magnitudes, identified as potential precursors, were clustered using the application of density-based spatial clustering of applications with noise (DBSCAN, Ester et al., 1996; Lehmann et al., 2020). Within the DBSCAN framework, a radius of 120 km was selected to define neighboring grid cells, as it was found to generate regions of reasonable sizes and spatial separation. The top six clusters with the maximum grid points were selected for further analysis. The clustered regions named as regions A to F are in decreasing order of number of grids in a cluster (Table S1 in Supporting Information S1), with clustered region A being the largest for a particular variable.

Step 3: Identification of teleconnections links and time lags.

For each selected clustered region for each climate variable, a time series was created by calculating the spatial average for individual clusters. This procedure reduces the data's dimensionality but preserves the spatiotemporal patterns (Kretschmer et al., 2017). Using CENs, we calculated the strength and temporal lags between the time series of six selected regions (clusters) for each variable (T2m, Z500, and WD) and FD-pc in all three study regions. Like previous analysis, time lags of 0–7 weeks were explored with a statistical significance of $p < 0.01$. In this step, we considered only links from climate variables toward FD-pc and removed all links emerging from FD-pc. By doing this, the potential factors will cover all the possible drivers of FD from different locations over the quasi-globe.

2.4. Predicting FD Using Machine Learning With CEN-Identified Drivers

After identifying regions that drive FD-pc using CEN analysis, we selected T2m, Z500, and WD time series over regions demonstrating significant direct causal links for predicting FD (Figure S5 in Supporting Information S1) using Random Forest (RF) model (Breiman, 2001). The predictions focus on both major FD events over each study region and FD occurrence spatially at each grid point over each study region. Here, we classified major (1) and non-major (0) FD events using weekly values of FD-pc depending on whether the percentage of FD coverage exceeded one standard deviation above the mean or not (Mo and Lettenmaier, 2015, 2016). Since there are fewer significant events (exceeding 1SD above the mean in the FD-pc binary data set) compared to the non-significant events, a classification algorithm directly leads to high accuracy in predicting the majority class (low FD-pc) but fails to capture the minority class (high FD-pc) adequately. To mitigate this issue, we applied the Synthetic Minority Oversampling TEchnique (SMOTE, Chawla et al., 2002) to the training data set. SMOTE operates within the feature space rather than the data space by generating synthetic minority class samples along the link between each minority class instance and its specific number of neighbors of the same class (Fernández et al., 2018; He & Garcia, 2009). The RF models were implemented using scikit-learn Python library and trained using 100 estimators (representing the number of trees in the forest) with the oversampled data set, and the maximum number of features evaluated at each tree node was determined as the square root of the total number of features. The data was divided into 70% for training and 30% for testing set. The feature importance was quantified based on Gini impurity (Breiman, 2001).

2.5. Evaluation Metrics

The evaluation of FD predictions involves a comprehensive analysis of the RF model's performance in distinguishing between drought and non-drought conditions. It requires a nuance understanding of various factors such as sensitivity, specificity, and overall predictive accuracy. We have used two prominent evaluation metrics to evaluate FD prediction model effectively up to a 4-week in advance, which are Receiver Operating Characteristic (ROC) curve and the Precision-Recall (PR) curve. The Area Under the Curve (AUC) for both ROC and PR

19447973, 2024, 11, Downloaded from https://agupubs.onlinelibrary.wiley.com/doi/10.1029/2024WR038391 by Auburn University Libraries, Wiley Online Library on [24/02/2025]. See the Terms and Conditions (https://onlinelibrary.wiley.com/terms-and-conditions) on Wiley Online Library for rules of use; OA articles are governed by the applicable Creative Commons License

curves further quantifies the overall performance, providing a comprehensive measure of a model's predictive accuracy in the context of FD forecasting. Below we briefly explain these skill measures.

The parameters used for calculating these metrices are true positive ($T_{Positive}$) value, True negative ($T_{Negative}$) value, False positive ($F_{Positive}$) value, and False negative ($F_{Negative}$) value. For our model evaluation, the $T_{Positive}$ value indicates the number of FD occurrences the model predicts correctly. $T_{Negative}$ value indicates the number of FD non-occurrences the model predicts correctly. $F_{Positive}$ value indicates the number of FD occurrences the model predicts incorrectly, that is, predicts the FD when there is no FD. $F_{Negative}$ value indicates the number of FD non-occurrences the model predicts incorrectly, that is, does not predict FD when there is FD.

A receiver operating characteristic (ROC) curve is constructed by plotting the $T_{Positive}$ rate versus the $F_{Positive}$ rate at various thresholds. Each point on the curve represents a different classification threshold, ranging from 0 to 1. The model shows higher accuracy if the ROC curve is toward the upper-left-hand corner and lower accuracy if the curve is closer to the 45° diagonal line in the ROC space. The area under the ROC curve (AUC_{ROC}) is a summary index of the model's skill for predicting the FD. An AUC score of 0 means the model's probability of predicting FD is 100% wrong, a score of 0.5 suggests that the model's ability to discriminate between the FD event and non-FD event classes is no better than random guessing, scores greater than 0.5 indicate that the model has a predictive capacity above random chance, with its ability to distinguish between classes improving as the score approaches 1. A score of 1 means the model's probability of predicting FD event is 100% correct. Therefore, an AUC_{ROC} score greater than 0.5 is generally considered an indication of a model's useful predictive performance, with higher scores reflecting higher accuracy in distinguishing between the classes.

The Precision-Recall (PR) curve has frequently been employed as complementary to ROC curves for evaluating the performance of binary classification models (Davis & Goadrich, 2006). When confronted with imbalanced data sets where the minority class is of particular interest, PR curves have proven to be an effective means of enhancing the statistical assessment of algorithm performance (Saito & Rehmsmeier, 2015). In PR space, recall versus precision is plotted at various thresholds; Recall (RC) is defined as the $T_{Positive}$ rate. Precision (PC) is a metric used to quantify the proportion of FD events accurately identified as positive among all FD events classified as positive, indicating the model's ability to predict the positive class accurately. In the context of performance evaluation in precision-recall (PR) space, models are deemed more accurate when their corresponding PR curves approach the upper-right-hand corner. Conversely, the models are considered less accurate when the curves approach a low-precision horizontal line. The area under the PR curve (AUC_{PR}) provides another summary index for evaluating model's predictive skill to identify FD. The AUC_{ROC} evaluates a model's ability to distinguish between classes, emphasizing the trade-off between sensitivity ($T_{Positive}$ rate) and specificity (1 - $F_{positive}$ rate) across all thresholds and performs well with balanced data sets. In contrast, the AUC_{PR} focuses on the trade-off between precision (the proportion of true positives among positive predictions) and recall ($T_{Positive}$ rate), making it more informative for imbalanced data sets, where positive class instances are rare or more important to identify accurately.

3. Results

Based on the FD definition using weekly RZSM during the warm season (see Methods), we identified the total number of FD events occurring at different grid points in the US over 36 years (1982–2018) (Figure 1a). Figure 1b shows the variation for FD percentage of coverage (FD-pc) in three study regions: SAG, UM, and ULC. A maximum of ∼37%, 36%, and 41% (and a minimum of zero) of the region in SAG, UM, and ULC has experienced FD in a single week, and 13, 8, and 16 events, respectively have occurred over the study period having FD-pc greater than 30%. We use FD-pc because it can represent both the magnitude and spatial extent of FD. The mean of all FD-pc was observed to be ∼7% for all three regions. For warm period (April–September), the variation of FD-pc shows that more FD are observed in May, April, and June for South Atlantic-Gulf (SAG), UM and Upper and lower Colorado (ULC) river basins respectively (Figure S1 in Supporting Information S1).

3.1. Causal Maps of U.S. FDs

The causal maps of three study regions: SAG, UM, and ULC river basins (Figure 1a) show the causal strengths (see Methods) between FD-pc and each climate variable, including 2-m air temperature (T2m), geopotential height at 500-hPa (Z500), and WD are presented in Figure 2. In SAG river basin region (Figures 2a–2c), T2m shows the strongest causal associations with FD-pc from the southeast US (SEUS ∼0.27) and western north

10.1029/2024WR038391

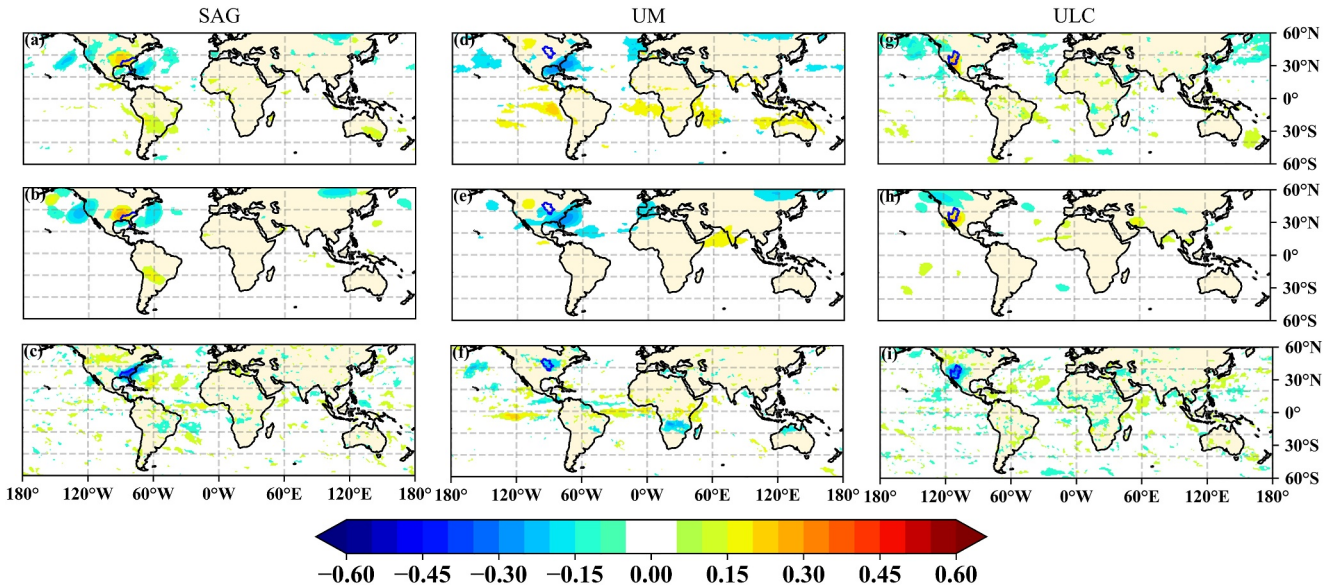

Figure 2. Causal analysis map of T2m (a, d, g), Z500 (b, e, h), and water deficit (c, f, i) at each grid point with FD-pc in South Atlantic Gulf (left column), upper Mississippi (middle column), and and upper and lower Colorado (right column) basin region (blue contour region). The maps show the highest causal strength (teleconnection index → FD-pc) between no lag to 7-week lag. Insignificant values at 99% confidence level and a magnitude <0.05 are removed.

Atlantic region (∼−0.26), as well as strong negative causal associations from Russia and central South America and a positive causation from southern Australia. Similar to T2m, for Z500, the prominent causal regions are mainly in the north subtropical regions, Russia and central South America. For WD, the most significant causal associations with FD-pc are from SEUS and the central North Atlantic Ocean. In the UM river basin region (Figures 2d–2f), positive causal relations from T2m occurs mainly between equator and 30°S in the southern hemisphere and negative relations in the northern hemisphere, especially in the Atlantic Ocean near SEUS and the Pacific Ocean near central south America. Significant causal associations with Z500 are from the SEUS, the tropics of the Indian and Atlantic Oceans, areas affected by the IOD and El Niño-Southern Oscillation, with additional influences from Russia and Spain regions. WD in the UM region drives FD in this region, with additional causal influences from the north central Pacific and equatorial Atlantic and Pacific regions. For ULC river basin (Figures 2g–2i), causal associations with FD-pc are observed for T2m from the north Pacific Ocean and Tasman Sea. For Z500, the causal associations with FD-pc are mainly from northern North America, with additional influences from the Bay of Bengal and southern Iran regions. The FD in ULC shows strong causal associations with T2m, Z500, and WD in the same region. Causation for WD shows heterogeneous global patterns, including influences from the Arabian Sea, Atlantic, and Pacific Ocean regions.

For global temperature, we have also examined the causal associations of FD-pc with global SST (besides T2m) for all three study regions individually (Fig. S2 in Supporting Information S1), given that SST in Indian, Pacific, and Atlantic oceans are associated with FDs via Rossby wave trains (DeAngelis et al., 2020; McIntosh & Hendon, 2018). It can be noted that the causal maps over oceans in all three study regions for SST (Figure S2 in Supporting Information S1) and T2m (Figures 2a, 2d, and 2g) are almost similar. For example, the Northeast Pacific and Northwest Atlantic Ocean regions in SAG and UM; equator to 30°S for UM; and the North Pacific and North Atlantic Ocean region for ULC. However, the results are not as prominent as T2m; the strength of causal associations is more than 0.2 for T2m and less than 0.15 for SST. Since T2m is also captured over land, we observed the influence of T2m from southeast US, central south America, California, a part of Russia, and southeast Australia for SAG (Figure 2a); southeast US, southern Australia, India, and a part of northern North America for UM (Figure 2d); and Colorado and part of British Columbia in Canada for ULC region (Figure 2g), which cannot be observed for SST. Additionally, various studies have found an influence of SST over SM and FDs for specific events (Mo & Lettenmaier, 2015; Schubert et al., 2021; Wang et al., 2014), but for FDs (a subseasonal phenomenon), the influence of SST seems not prominent (relative to T2m). This can be because SST has a long-term memory and is resistant to sudden change due to relatively slow circulation systems (Dangendorf

19447973, 2024, 11, Downloaded from https://agupubs.onlinelibrary.wiley.com/doi/10.1029/2024WR038391 by Auburn University Libraries, Wiley Online Library on [24/02/2025]. See the Terms and Conditions (https://onlinelibrary.wiley.com/terms-and-conditions) on Wiley Online Library for rules of use; OA articles are governed by the applicable Creative Commons License

et al., 2014). These observations made T2m a better variable for analyzing causal associations for subseasonal FD-pc.

3.2. Causal Links Between U.S. FDs and CEN Discovered Causal Regions

The clustered regions around the globe for T2m, Z500, and WD influencing FD-pc in SAG, UM, and ULC river basins are shown in Figures 3–5a–5c, (see Methods, step 2 of the model-building). With all these regions, the teleconnection links, their strength of causal influence (positive/negative), and lag times are shown in the CEN (CEN; Figures 3–5d–5f) of the areal averaged time series over the six prominent regions and FD-pc (see Methods, Step 3 of the model-building). Refer to Table 1 for teleconnection regions and Table S2 in Supporting Information S1 for strength of each causal link.

The SEUS region A has the strongest direct causal link with SAG FD (0.255) indicating that T2m increases in SEUS and nearby cause SAG FD (Figures 3a and 3d). Central South America (B) has a positive impact on SAG FD with a lag of 2 weeks, while the Northeast Pacific (E) shows a positive effect with a 1-week lag. A temperature rises in SEUS (A) and Central South America (B) amplifies SAG FD, while rise in Northwest Atlantic Ocean (C) and Northeast Pacific Ocean (E) reduce its occurrence. Region F from ULC and nearby affects region E at a 3-week lag, which then impacts SAG FD in 1 week. Eastern Russia's region D influences region C, which directly and indirectly (through A) influences SAG FD-pc. Every Z500 region except C (near North Pacific Ocean) have direct causal links to SAG FD-pc (Figures 3b and 3e). The strongest positive causal link is from region D in SEUS (0.249) at no lag and same region shows negative link at 3 weeks lag to SAG FD. Region F in Central South America and Region E in Eastern Russia has a direct positive and negative causal links at a two and 1-week lag. Region A in Northeastern Pacific and California has a direct negative link at a 1-week lag. The WD cluster from region A in SEUS is the largest and has the strongest direct negative influence on FD-pc in SAG with a strength of −0.427 and −0.286 at zero- and 1-week lag, respectively (Figures 3c and 3f). Region B in the northwest US and E in the Equatorial Atlantic Ocean have a direct positive link with SAG FD at zero lags. Region C in the Southern Atlantic and D in the Northwest Atlantic Ocean have indirect positive links via E at 4 and 1 week lag, respectively.

For UM region FD-pc, the T2m from Northwest Atlantic region (A) have direct negative link at zero lag (Figures 4a and 4d, Table 1). T2m region B (near Northern Australia) and D (near Southeast Pacific Ocean) influence temperature in region E (near Northeast Pacific Ocean) at a 6-week and 0-week lag, respectively, which finally influences UM FD at 4 and 6 weeks lag equally (Figure 4d). Thus, there will be a 10- to 12-week lag for T2m in B to influence UM FD. Z500 from regions A (in Northwest Atlantic and SEUS) and E (near North central Atlantic) has a direct negative link at zero- and 1-week lag, respectively (Figures 4b and 4e). Region B from eastern Russia has a direct negative and positive causal link at zero- and 7-week lag. Region F near northwest US strongly influences UM FD (0.215) at a 1-week lag. North Indian Ocean (C) has an indirect link through A at 1 week lag. WD from UM & nearby regions (E) has a strongest negative causal influence on UM FD (−0.297) at week zero and an additional link at 1 week lag (Figures 4c and 4f). Northeast Pacific Ocean region (D) has a negative causal link at 1 week lag. Equatorial east-Pacific (A) and Equatorial Atlantic Ocean region (B) have a direct positive link. The negative link suggests that a decrease in WD in these areas can increase FD in UM or vice versa.

For ULC FD-pc, T2m from regions A, D, and E are observed to have a direct link (Figures 5a and 5d, Table 1) with E in ULC & nearby regions having the highest causal strength (0.308) at zero lag but link is contemporaneous that is, directionality is undecided due to conflicting orientation rules (Runge, 2020). Regions B, C, and F have indirect positive causal link to ULC FD via A or E (refer to Figure 5 or Table 1 for locations). Z500 from regions B, D, and F have a direct positive causation at zero, five, and 7-weeks lag (Figures 5b and 5e) suggesting that the time lag from a region is distance dependent. Regions A and E have a direct negative causation at a lag of one and 0 weeks, with ULC FD. WD regions, all six regions have direct link with ULC FD-pc (Figures 5c and 5f), suggesting that WD from these regions can amplify or reduce FD-affected regions in ULC. Regions A, B, D, and F have negative causal links at a lag of 0, 4, 1, and 4 weeks, respectively and regions C and E have positive causal links at 4 and 1-week lag, respectively.

3.3. CEN Discovered Sources of Causations Predict U.S. FDs

We forecast FD events using the RF algorithm by leveraging the direct CEN links to FD-pc (see Methods). The locations of all these regions are summarized in Figures 3–5.

19447973, 2024, 11, Downloaded from https://agupubs.onlinelibrary.wiley.com/doi/10.1029/2024WR038391 by Auburn University Libraries, Wiley Online Library on [24/02/2025]. See the Terms and Conditions (https://onlinelibrary.wiley.com/terms-and-conditions) on Wiley Online Library for rules of use; OA articles are governed by the applicable Creative Commons License

10.1029/2024WR038391

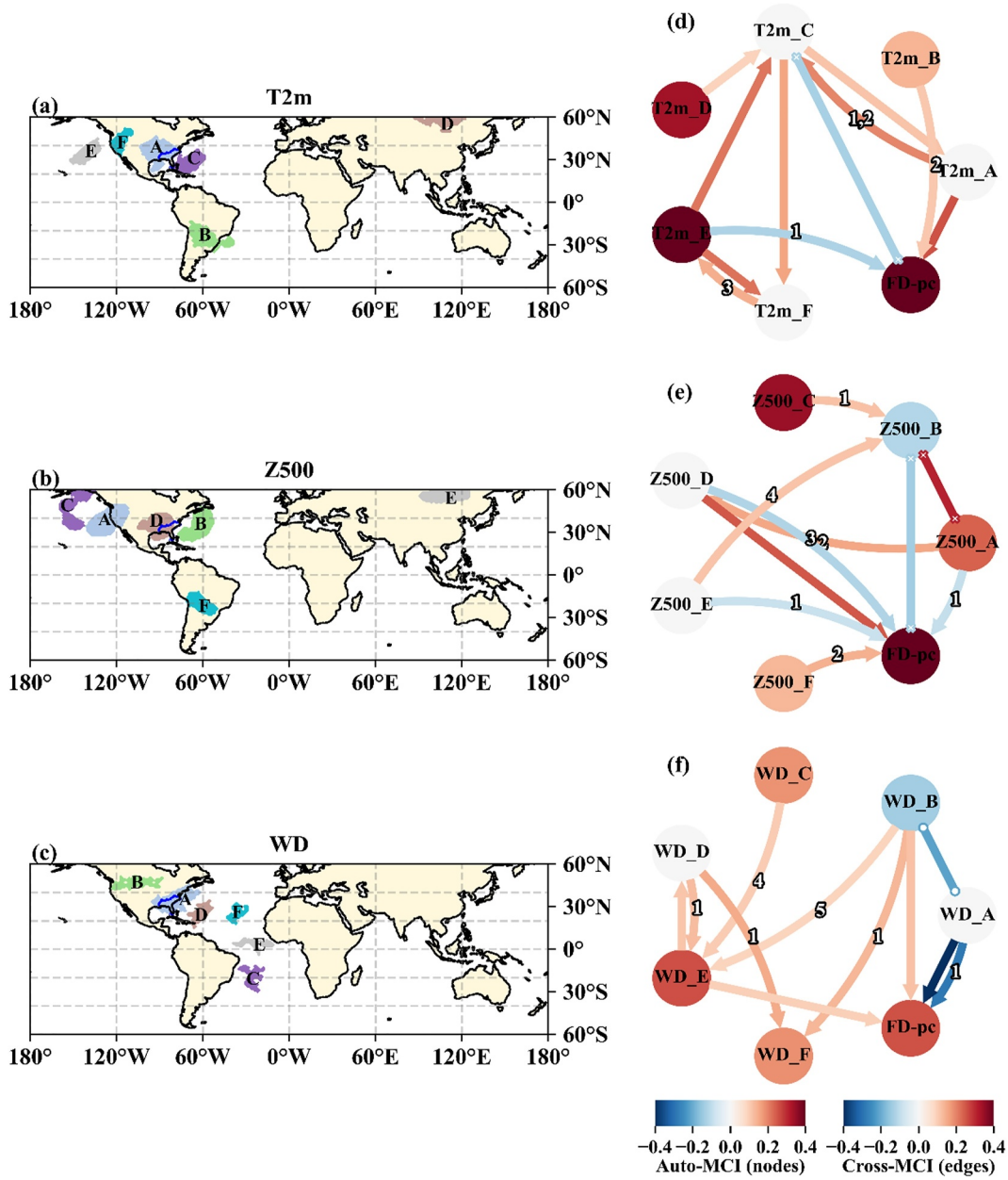

Figure 3. Left column figure (a–c) shows six prominent and larger regions of causal maps selected regions using DBSCAN algorithm. Right column figure (d–f) shows causal effect network built with area averaged timeseries of six different regions selected for T2m (a, d), Z500 (b, e), and water deficit (c, f) with FD-pc in South Atlantic-Gulf River basin (with $p < 0.01$) and up to 7-week lag for period 1982–2018. The names in the nodes represent the climate variable followed by the region as suffixes. The color of an arrow or node represents the strength of the cross- or auto-dependency, respectively. All auto-dependencies have a time delay of $\tau = 1$. Arrows with cross at ends represent conflicting contemporaneous links (directionality is undecided due to conflicting orientation rules). Arrows with circles at ends represent unoriented, contemporaneous links (collider and orientation rules could not be applied). Numbers on arrow demonstrate lag period for maximum strength of causal link (no number meaning no lag).

The ROC curve in Figures 6a–6c shows the RF model's performances based on actual direct links to FD-pc lags shown in CENs (Figures 3–5) for classifying the major FD-pc events (see Methods). The RF classifier model built on T2m, Z500, and WD regions showing direct global teleconnections for FD-pc shows a high AUC_{ROC} score of 0.806, 0.796, and 0.740 in SAG, UM, and ULC regions, respectively, for predicting the major FD-pc class in the

19447973, 2024, 11, Downloaded from https://agupubs.onlinelibrary.wiley.com/doi/10.1029/2024WR038391 by Auburn University Libraries, Wiley Online Library on [24/02/2025]. See the Terms and Conditions (https://onlinelibrary.wiley.com/terms-and-conditions) on Wiley Online Library for rules of use; OA articles are governed by the applicable Creative Commons License

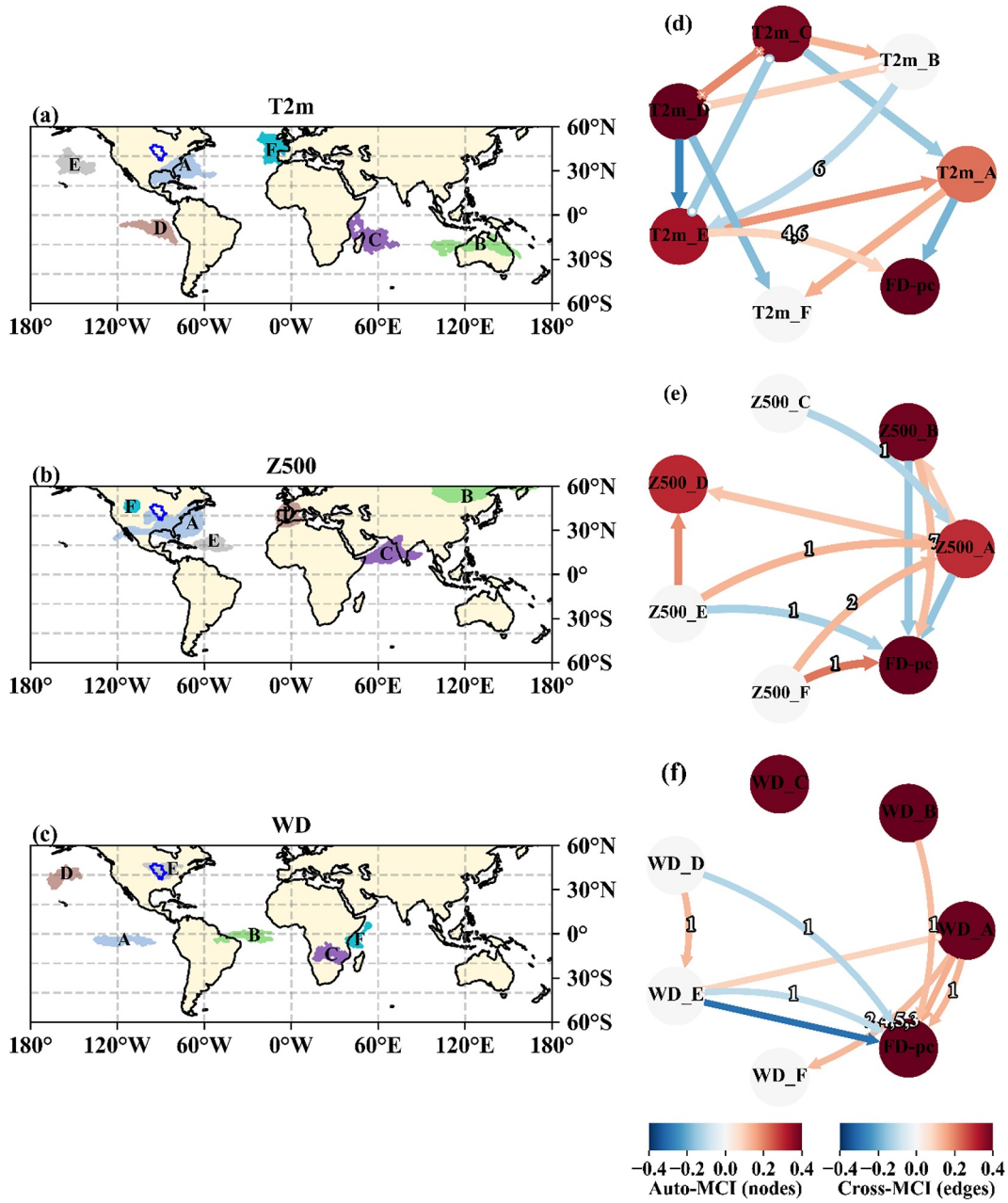

Figure 4. Same as Figure 3, but for upper Mississippi River basin region.

test set. Figures 6d–6f shows a precision-recall (PR) curve with an AUC_{PRC} of 0.966, 0.950, and 0.937 for SAG, UM, and ULC regions, respectively.

Regions (of T2m, Z500, and WD regions showing direct global teleconnections) used in the RF model are arranged in decreasing order of variable importance, that is, their influence in accurately classifying the FD-pc (Figures 6g–6i). For SAG FD prediction (Figure 6g), WD from region A in SAG contributes the most to FD occurrence in SEUS, followed by WD from region E in the equatorial Atlantic Ocean. For T2m and Z500, region B in central South America and region F from central South America have a higher influence than all other locations (Figure 3). For UM FD prediction (Figure 6h), WD from region B in the Equatorial Atlantic Ocean contributes the most, followed by WD from region A in the Equatorial East-Pacific. Both variables, T2m and Z500, the greater influence is observed from common region A in Northwest Atlantic Ocean which has maximum grid points in the cluster (Figure 4). Regarding ULC FD modeling (Figure 6i), T2m from region A in the Northeast

19447973, 2024, 11, Downloaded from https://agupubs.onlinelibrary.wiley.com/doi/10.1029/2024WR038391 by Auburn University Libraries, Wiley Online Library on [24/02/2025]. See the Terms and Conditions (https://onlinelibrary.wiley.com/terms-and-conditions) on Wiley Online Library for rules of use; OA articles are governed by the applicable Creative Commons License

10.1029/2024WR038391

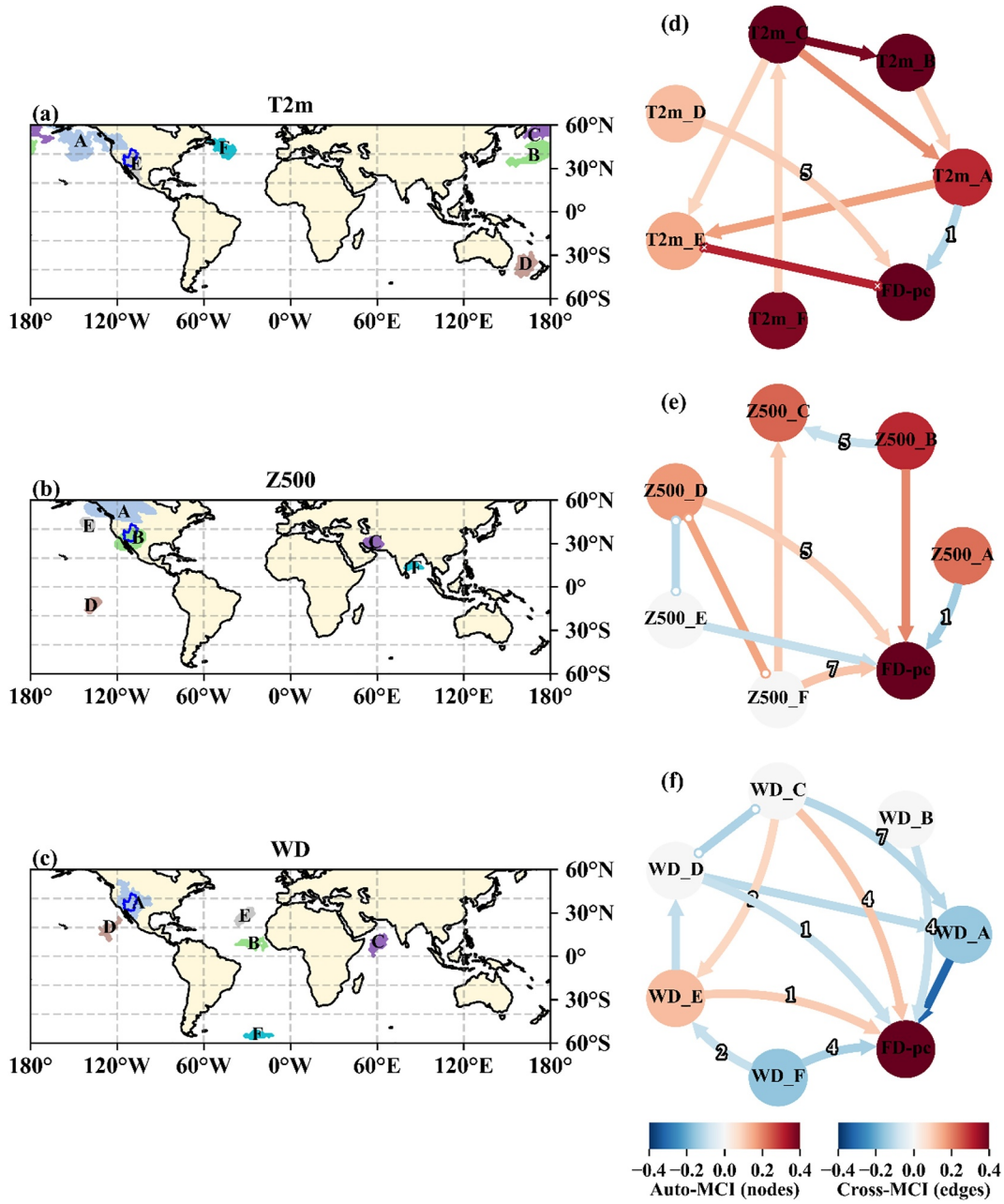

Figure 5. Same as Figure 3, but for upper & lower Colorado River basin region.

Pacific Ocean and E in the Northwest Atlantic Ocean have a strong influence. For Z500 and WD, region A in Southwest Canada and region C in the north Indian Ocean has relatively stronger influences on FD prediction in ULC among all six analyzed regions (Figure 5).

We obtained the results of the AUC_{ROC} score for predicting FD over the space from weeks 1–4 in advance using the same RF model, as shown in Figure 7. The results show that the prediction is skilful up to 4-week lead time, with spatial average ROC score of 0.544, 0.669, and 0.608 for SAG, UM, and ULC regions. Notably, the SAG region, particularly around Florida, demonstrates a higher prediction accuracy compared to the other regions. In the UM region, predictions are highly accurate (ROC > 0.8), especially in the northeast, maintaining this accuracy up to 3 weeks. At a 4-week lead, the northeast still exhibits relatively high ROC scores, whereas the central UM region, the score increased at week 4 after an observed lower ROC score during the second and third weeks. At a

19447973, 2024, 11, Downloaded from https://agupubs.onlinelibrary.wiley.com/doi/10.1029/2024WR038391 by Auburn University Libraries, Wiley Online Library on [24/02/2025]. See the Terms and Conditions (https://onlinelibrary.wiley.com/terms-and-conditions) on Wiley Online Library for rules of use; OA articles are governed by the applicable Creative Commons License

19447973, 2024, 11, Downloaded from https://agupubs.onlinelibrary.wiley.com/doi/10.1029/2024WR038391 by Auburn University Libraries, Wiley Online Library on [24/02/2025]. See the Terms and Conditions (https://onlinelibrary.wiley.com/terms-and-conditions) on Wiley Online Library for rules of use; OA articles are governed by the applicable Creative Commons License

Table 1
Approximate Locations of the Significant Teleconnection Regions Observed in Figures 3–5 for the South Atlantic Gulf, Upper Mississippi, and Upper and Lower Colorado River Basins Respectively in the World Map

Regions	T2m	Z500	WD
SAG River basin teleconnection regions			
A	Southeastern US	Northeastern Pacific & California	Southeastern US
B	Central South America	*Northwest Atlantic Ocean*	Northwest US
C	*Northwest Atlantic Ocean*	North Pacific Ocean	Southern Atlantic
D	Eastern Russia	Southeastern US	Northwest Atlantic Ocean
E	Northeast Pacific Ocean	Eastern Russia	Equatorial Atlantic Ocean
F	ULC & nearby regions	Central South America	Northcentral Atlantic Ocean
UM River basin teleconnection regions			
A	Northwest Atlantic Ocean	Northwest Atlantic and SEUS	Equatorial east-Pacific
B	Northern Australia	Eastern Russia	Equatorial Atlantic Ocean
C	Southwest Indian Ocean	North Indian Ocean	South Africa
D	Southeast Pacific Ocean	Spain & nearby regions	Northeast Pacific Ocean
E	Northeast Pacific Ocean	North central Atlantic	UM & nearby regions
F	Northeast Atlantic Ocean	Northwest US	Western equatorial Indian ocean
ULC River basin teleconnection regions			
A	Northeast Pacific Ocean	Southwest Canada	ULC & nearby regions
B	Northcentral Pacific Ocean	ULC & nearby regions	Equatorial Atlantic Ocean
C	North Pacific Ocean	Iran	North Indian Ocean
D	Tasman Sea	Central south Pacific Ocean	Northeastern Pacific Ocean
E	*ULC & nearby regions*	Northeast Pacific Ocean	Central north Atlantic Ocean
F	Northwest Atlantic Ocean	North Indian Ocean	Southern Atlantic Ocean

Note. Teleconnection regions are denoted in different colors based on causal links to FD-pc: red (direct positive), blue (direct negative), green (both positive and negative link at different lead times), and black (no direct link, indirect link might be present). Italic fonts in the table show contemporaneous causal link to FD-pc.

1-week lead, the entire UM region demonstrates excellent predictive performance with a ROC score of 0.721. The model performed more accurately in the UM region (0.669) at a 4-week lead compared to the 1-week leads in SAG (0.621) and ULC (0.655). In the ULC region, the eastern and northern areas consistently exhibit ROC scores above 0.70 across all 1–4-week lead times. The central ULC area also demonstrates higher ROC scores during the first 2 weeks, with a decline in the third week, followed by a slight increase in the fourth week.

4. Discussion

In this study, we revealed global causal sources of FD in three river basins over the US using causal discovery framework. The results identified causal regions that align with established teleconnection sources or reveal potential new sources, as summarized in Table 2. Moreover, using identified FD driving regions, the ML model can well predict U.S. FDs up to 4 weeks in advance, which confirmed the usefulness of the discovered teleconnection links and their capability for predicting extreme events. In the following paragraphs, we attempted to corroborate our results with previous studies and interpret the probable reasons for causations, as indicated by causal maps and CENs from various global regions (Table 2).

Regions A–D (Figure 3b) for Z500 (and E, F, A, and C for T2m; Figure 3a) are observed to influence FD-pc in SAG on the weekly timescale. They might be linked via a wave train of positive and negative values (~±0.2) spanning the regions from the North Pacific Ocean to the North Atlantic Ocean via North American landmass. These regions generate a wave train response of low and high temperature/pressure systems over the northwestern region (Sellars et al., 2017) that powers FDs over the SAG region. These semi-permanent Pacific/North American

10.1029/2024WR038391

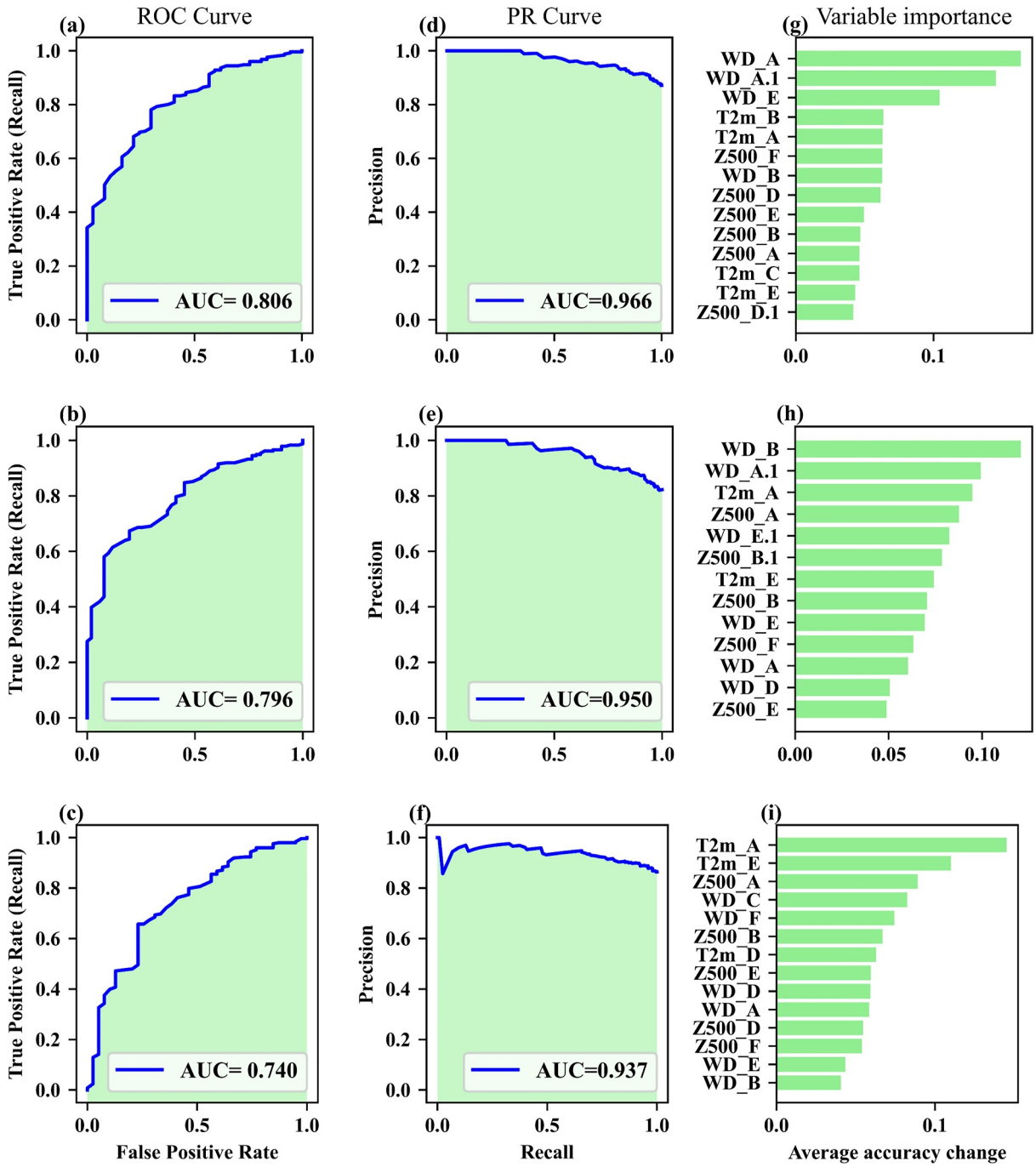

Figure 6. The Receiver Operating Characteristic curve (a–c), PR curve (d–f), and Evaluation of variable importance (g–i) for the Random Forest (RF) model at actual time lags as observed on direct links of causal effect networks (CENs) between all three climate variables (T2m, Z500 and water deficit) and FD-pc (Figure 3) for higher FD-pc classification on the test data set in South Atlantic Gulf, upper Mississippi, and upper and lower Colorado river basins. The *x*-axis in figure g shows the decrease in average accuracy among all trials and *y*-axis shows the variables ordered from top-to-bottom as most-to-least important in classifying major FD-pc events. Number Suffixes at the end of region name denotes week lag considered in our RF model obtained from CEN (Figure 3). Figure h is same as g but using direct links from Figure 4 for UM River basin. Figure (i) is same as g but using direct links from Figure 5 for upper & lower Colorado River basin.

(PNA) patterns, along with Quasi Biennial oscillations (QBO), may interact and propagate with jet streams, which can cause changes in SM in SEUS regions.

Furthermore, for T2m, region E in Figures 3a and 4a and regions A & C in Figure 3b are influenced by extreme Pacific patterns during the warm period and show association with high temperatures and droughts in the eastern

19447973, 2024, 11, Downloaded from https://agupubs.onlinelibrary.wiley.com/doi/10.1029/2024WR038391 by Auburn University Libraries, Wiley Online Library on [24/02/2025]. See the Terms and Conditions (https://onlinelibrary.wiley.com/terms-and-conditions) on Wiley Online Library for rules of use; OA articles are governed by the applicable Creative Commons License

10.1029/2024WR038391

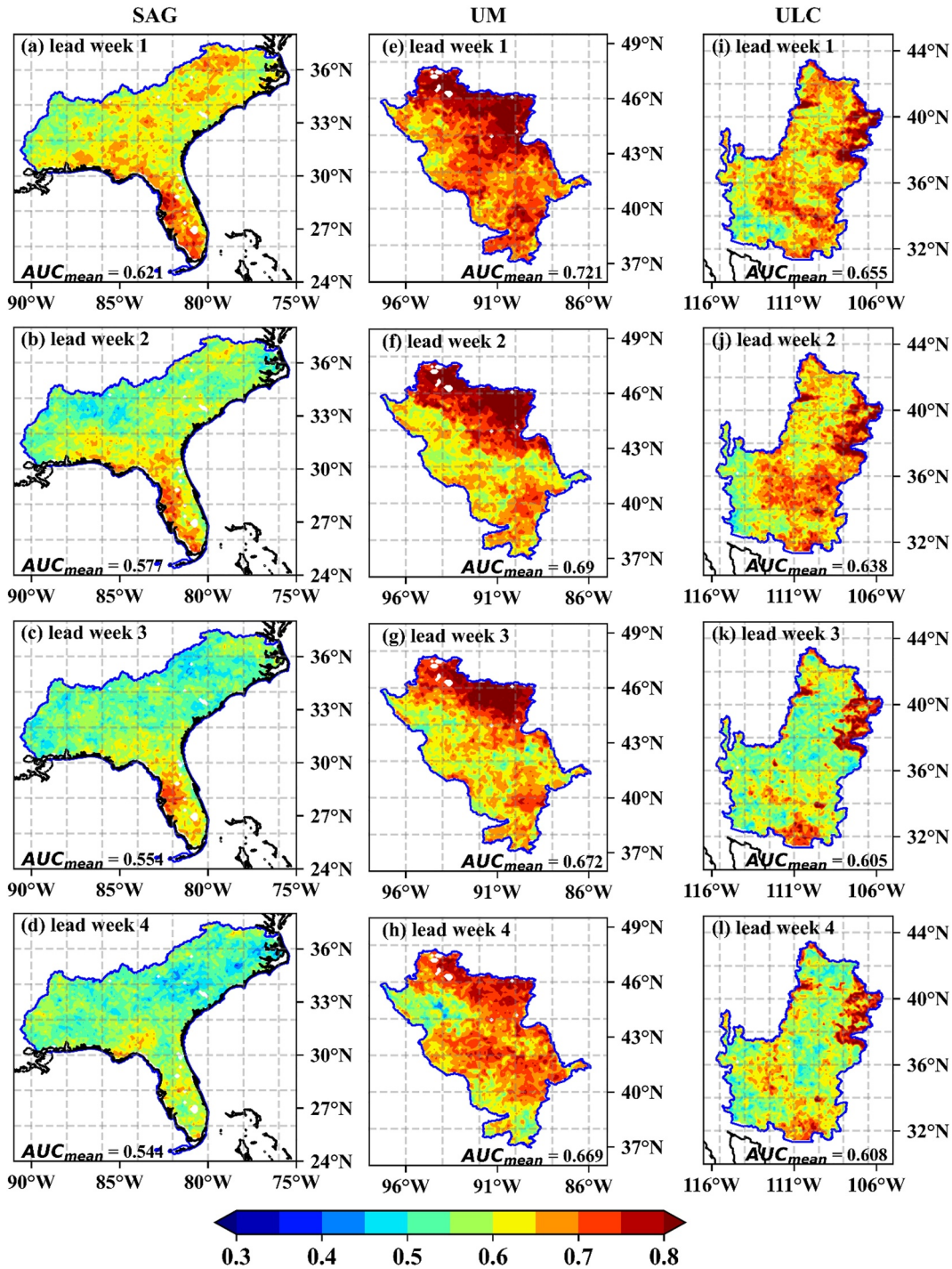

Figure 7. Area Under the Curve (AUC) score of the Receiver Operating Characteristic curve for predicting flash drought at each grid points of the South Atlantic-Gulf (a–d), upper Mississippi (e–h), and upper & lower Colorado (i–l) from lead week 1 to week 4. Average of AUC score of all grid points at each lead time is noted in each map.

US (McKinnon et al., 2016). Our findings of T2m region A, Z500 region D, and WD region A for SAG (Figure 3) and T2m region A, Z500 region A, and WD region E for UM (Figure 4) are consistent with Ford and Labosier (2017) at similar time lags, which provided detailed reasons for these atmospheric variables causing rapid SM desiccation in the eastern US. Drier conditions (WD region A in Figures 3c and 5c) are driven by increased

19447973, 2024, 11, Downloaded from https://agupubs.onlinelibrary.wiley.com/doi/10.1029/2024WR038391 by Auburn University Libraries, Wiley Online Library on [24/02/2025]. See the Terms and Conditions (https://onlinelibrary.wiley.com/terms-and-conditions) on Wiley Online Library for rules of use; OA articles are governed by the applicable Creative Commons License

19447973, 2024, 11, Downloaded from https://agupubs.onlinelibrary.wiley.com/doi/10.1029/2024WR038391 by Auburn University Libraries, Wiley Online Library on [24/02/2025]. See the Terms and Conditions (https://onlinelibrary.wiley.com/terms-and-conditions) on Wiley Online Library for rules of use; OA articles are governed by the applicable Creative Commons License

Table 2
Identified Causal Regions for Flash Droughts of the Three River Basins, Including Findings Confirming With Previous Studies (References Cited), Required Further Investigations, or Explained in the Discussion Section

Regions	T2m	Z500	WD
SAG River basin teleconnection regions			
A	Ford and Labosier (2017)	McKinnon et al. (2016)	Ford and Labosier (2017)
B	Refer to discussions	Luo et al. (2021)	Refer to discussions
C	Refer to discussions	McKinnon et al. (2016)	Further investigation needed
D	Clark and Feldstein (2022)	Ford and Labosier (2017)	Luo et al. (2021)
E	McKinnon et al. (2016)	Clark and Feldstein (2022)	Further investigation needed
F	Refer to discussions	Refer to discussions	No direct/indirect link to FD-pc
UM River basin teleconnection regions			
A	Ford and Labosier (2017)	Ford and Labosier (2017); Luo et al. (2021)	Further investigation needed
B	Further investigation needed	Clark and Feldstein (2022)	Further investigation needed
C	Further investigation needed	Schubert et al. (2021)	No direct/indirect link to FD-pc
D	Further investigation needed	No direct/indirect link to FD-pc	Lesinger and Tian (2022)
E	McKinnon et al. (2016)	Luo et al. (2021)	Ford and Labosier (2017)
F	No direct/indirect link to FD-pc	Further investigation needed	No direct/indirect link to FD-pc
ULC River basin teleconnection regions			
A	Beaudin et al. (2023)	Ren et al. (2023); Vijverberg and Coumou (2022)	Refer to discussions
B	Beaudin et al. (2023)	Further investigation needed	Further investigation needed
C	Beaudin et al. (2023)	No direct/indirect link to FD-pc	Schubert et al. (2021)
D	Further investigation needed	Further investigation needed	Dettinger (2013)
E	Refer to discussions	Ren et al. (2023); Vijverberg and Coumou (2022)	Further investigation needed
F	Further investigation needed	Schubert et al. (2021)	Further investigation needed

evapotranspiration from rising temperatures. Reduced water availability forces tradeoffs between competing water use, including agriculture, ecosystems, and urban areas.

The T2m of region A (SEUS) in Figure 3a and region E (ULC) in Figure 5a positively influence FD in respective regions. The warming in the US west coast and Eastern Pacific can induce change in vapor fluxes and reduce precipitation in the ULC are impacted by northeast Pacific temperatures (Beaudin et al., 2023) indicated as T2m region A at 1 week lag, which is influenced by region B and C (Figures 5a and 5d). The cooler temperatures along the US West Coast and hotter in the central Northeast Pacific decrease the extent of moisture transported over ULC, thus increasing WD. These vapor fluxes are driven by large-scale changes in the wind associated with the atmospheric adjustment to the strong North Pacific SST (Beaudin et al., 2023).

Region B (Figure 3b) and A/E (Figure 4b) negatively influence SAG and UM FD can be attributed to the moving Bermuda high-pressure system, which sits over the Atlantic Ocean in the summer (Luo et al., 2021). This high-pressure system influences moisture transport to the SAG and UM regions. A similar mechanism is also observed for region D of Figure 3c. The moisture from the Gulf of Mexico and the equatorial Atlantic Ocean is transported to SAG as the Bermuda high is far enough east; the resulted wind direction is perfect for bringing in a large amount of moisture and heat to the eastern USA.

The region C in Figure 4b and C in Figure 5c/F in Figure 5b influence FD in UM and ULC, respectively, by positive IOD. Various studies suggested that IOD, along with tropical pacific ENSO events, influences the temperature and precipitation in the US through the Rossby wave train and contributes to making them drier (McKinnon et al., 2016; Mo & Lettenmaier, 2016; Schubert et al., 2021). For WD, regions A in Figure 3c, E in Figure 4c, and A in Figure 5c are just above the study region, and it can be observed that WD causes FD in the region. Moreover, WD regions B and D influence SAG FD (Figure 3c) by deep convection from both sides. It was

19447973, 2024, 11, Downloaded from https://agupubs.onlinelibrary.wiley.com/doi/10.1029/2024WR038391 by Auburn University Libraries, Wiley Online Library on [24/02/2025]. See the Terms and Conditions (https://onlinelibrary.wiley.com/terms-and-conditions) on Wiley Online Library for rules of use; OA articles are governed by the applicable Creative Commons License

also noted that for WD, these regions may not have enough time to adapt to the sudden onset of large WDs and heat extremes (Deng et al., 2022; Yuan et al., 2023) when more frequent FDs are observed.

WD region D in the Northeastern Pacific Ocean near the California coast negatively influences FD-pc (Figure 5c) in the ULC region. Precipitation in ULC should be driven by moisture transport from region D through atmospheric rivers (ARs; Ralph & Dettinger, 2011), which increases the amount of precipitation in California and nearby regions (Dettinger, 2013). ARs are projected to increase with global warming (Wang et al., 2023) and will carry water vapor with them, increasing precipitation on the west coast and nearby, helping in reducing FD and drought events in ULC regions. Increased temperature in ULC will increase the Z500 in the region, causing low pressure there (Figure S3 in Supporting Information S1). Moreover, the moist air from regions A and E (Figure 5b) will also be transported to this region and will negatively affect (Figure 5e) the occurrence of FD in ULC. Warmer west coast SST during a positive Pacific Decadal Oscillation phase with reduced cold upwelling and increased net downward heat flux plays a role in moisture transport with low-level jet in ULC and nearby (Ren et al., 2023; Vijverberg & Coumou, 2022). The WD region D in Figure 4c in the Southeast Pacific Ocean is influenced by the study region's Pacific Decadal Oscillation associated with FD (Lesinger & Tian, 2022).

A diabatic heating source in South America could affect the SAG by exerting a low-level low anomaly in the northern tropical and SEUS. The low anomaly could counteract the climatological low-level atmospheric flow, reducing inland moisture transport and leading to precipitation deficits in the SAG. It suggests that T2m (region B) and Z500 (region F) in central South America (Figures 3a and 3b) are typically associated with atmospheric circulation forcings (e.g., diabatic heating)—the source for atmospheric teleconnection to SAG. This is confirmed by the 850 hPa anomaly wind pattern during warm period, showing a general direction from central South America to SEUS, with central South America having higher surface pressure than SEUS (Figure S3 in Supporting Information S1).

Consistent with our teleconnection observations from eastern Russia (region E in Figure 3b, D in Figure 3a, and B in Figure 4b), Clark and Feldstein (2022) concluded that eastern Russia and the eastern US are linked by PNA teleconnections and influence through advection of air temperature by the anomalous meridional wind and vertical mixing. Schubert et al. (2011) concluded that the observed wave pattern, characterized by its primary association with the leading 250-hPa zonal wind component, manifests initially within the North Atlantic jet stream. This wave undergoes bifurcation upon its departure from the jet stream axis. A significant fraction of the wave's energy is observed to propagate along a trajectory northward of the Eurasian jet, traversing over Northern Europe and Russia. In these regions, the wave considerably influences the spatiotemporal variability of surface meteorological parameters, notably temperature and precipitation. Subsequent wave exits exhibit a global span, with one such exit extending from the Indian subcontinent across to North America. The ensuing pathways, encompassing the third and fourth exits, originate from the eastern Pacific, stretching towards Europe. These wind pathways link the regions of Europe, Russia, the Indian subcontinent region, and the eastern Pacific. These trajectories are critically implicated in modulating the hydroclimatic conditions of North America (Schubert et al., 2011), denoting their significant impact on regional US precipitation and temperature patterns and, subsequently, the regional FDs.

Dry SM condition corresponds well to Z500 (Zhang et al., 2019) and WD (Deng et al., 2022; Mahto & Mishra, 2023; Wang & Yuan, 2022). The increased Z500 may raise downward solar radiation reaching the land surface and enhance subsidence warming, leading to relatively warmer T2m and warmer days. Higher Z500 may also decrease precipitation, resulting in drier soil. This drier surface soil leads to even greater sensible heat fluxes and greater heat entertainment (HE) into the planetary boundary layer (PBL). SHF and HE may further increase the T2m of the region. The higher PBL also helps to maintain the higher Z500. These conditions are favorable for the occurrence of FDs. It was observed that WD over the study region has the strongest influence on FD in these regions (Figures 3–5). Many previous studies also suggested WD to be a dominant reason for FD occurrence in the SAG region (Mahto & Mishra, 2023) and globally (Deng et al., 2022; Wang & Yuan, 2022). We observed stronger causal links from WD regions to FD-pc study region, while the WD far from the study region show minimal influence. Z500 from Russia in SAG and UM, or Z500 and WD from the north Indian Ocean in the ULC, has causal links over long distances that influence FD. There are a few contemporaneous links observed in the CEN analysis, which can be due to the conflicts of directionality or collider, and orientation rules could not be applied (Markov equivalence; Runge, 2020). The linkages considered to be contemporaneous on a weekly scale may be causal on a sub-weekly timescale. For instance, the conflicting link between region E of T2m and ULC

19447973, 2024, 11, Downloaded from https://agupubs.onlinelibrary.wiley.com/doi/10.1029/2024WR038391 by Auburn University Libraries, Wiley Online Library on [24/02/2025]. See the Terms and Conditions (https://onlinelibrary.wiley.com/terms-and-conditions) on Wiley Online Library for rules of use; OA articles are governed by the applicable Creative Commons License

FD-pc (Figure 5d) or the unoriented link for Z500 of region B with A or FD-pc in SAG (Figure 3e) may be considered causal on a different timescale. Malloy & Kirtman (2023) found that these links change to causal links on changing the analysis period, that is, in our case, less/more than 7 days.

For our model predicting FD, the high AUC values for PR and ROC curve suggest that the model is robust and can be used to identify the extent of any FD-pc in the future using T2m, Z500, and WD data from the identified regions and teleconnections. Here, it is worth noting that for SAG and UM, WD was the major variable for FD predictions; however, for ULC, T2m seems to be the major predictor. In other words, the surface temperature has more influence than WD (and Z500) for ULC FD occurrence; however, WD is the most influential variable for SAG and UM FD. Our results for AUC_{ROC} score (Figure 7) are consistent with Pendergrass et al. (2020); they indicated that the ability to predict drought events improves from the southern to the northern regions of the US. Overall, the ROC score generally decreases from the first to the fourth week across all regions, except for the ULC region, where the ROC score in the fourth week nearly equals to that of the third week due to the model's accurate predictions for the eastern ULC region at the 4-week lead. Consequently, these findings affirm the model's effectiveness in forecasting the potential scope of future FD events by leveraging T2m, Z500, and WD data from specific areas. Our model demonstrates improved prediction skills for all weeks 1–4 compared to previous FD forecast results. For instance, Su et al. (2023) showed that while predictions for the onset and end of major droughts in the Coastal Western U.S. were reliable at 1- and 2-week lead times, their accuracy declined significantly at 3 weeks, with no predictive skill beyond 4 weeks. Lesinger et al. (2024) demonstrated that the anomaly correlation coefficient for RZSM forecasts reaches nearly 0.6 for lead weeks 3–4. Accurate FD predictions allow operational agencies to issue early warning alerts, effectively helping to mitigate drought impacts. While subseasonal predictions offer the potential to inform users about impending extreme climate events, further research is needed to enhance the accuracy of FD predictions.

This study has several limitations that could be addressed in future studies. First, this study used regional RZSM simulations and global reanalysis data sets, which can be different from the ground SM and climate observations (Mishra et al., 2017). It requires improving SM and climate data for more accurate FD characterizations. Second, this study only considered SM at 40 cm for FD definitions, while the response of SM is closely related to soil depth, with moisture in deeper soil layers being relatively more stable and insensitive to short-term atmospheric changes (Li et al., 2020; Zhang et al., 2017). Therefore, the FD causal analysis and prediction results could be affected if FDs are analyzed at a different depth. Moreover, CEN was performed only based on four variables (T2m, SST, Z500, and WD). Additional known variables, for example, surface wind patterns and surface pressure may influence the FDs in the study areas (SAG, UM, and ULC), and their inclusion in CEN may find additional teleconnection regions. Utilizing the CEN and causal maps alongside model data makes it possible to uncover causal linkages that differ from what is observed, which would be valuable in understanding the model biases associated with these teleconnections. Additionally, large-scale climate oscillations strongly influence FD intensity and severity through teleconnections; many of them have been confirmed by evidence or past research; however, there are identified regions still require further investigations (See Table 2 for summary). This includes, (a) The influence of WD region C and E in the central and south Atlantic Ocean to SAG FD (Figure 3). (b) The link from T2m regions B, C, and D, Z500 region F and WD region A and B to UM FD (Figure 4). It can be noted that WD regions A, B, and F (Figure 4c) are near the equator (same for WD region E in Figure 3c), and summer ITCZ moving towards the east may show some teleconnection pattern. (c) The link from T2m regions D and F, Z500 region B and D, and WD regions B, E, and F to ULC FD (Figure 5). Moreover, other characteristics of FDs, like severity and duration may be explored extensively in future providing new insights.

While CENs are useful for identifying causal relationships between the potential drivers and FD, CENs still have limitations in fully capturing the complexity of climate system dynamics (Nowack et al., 2020). These systems involve intricate interactions and teleconnections, such as the global impacts of ENSO, which can be oversimplified by causal networks that focus on a subset of variables and linear relationships (Donges et al., 2009; Runge, Nowack, et al., 2019). The networks are also highly dependent on what variables and timescales are selected for analysis, meaning that omitting key drivers or using inappropriate temporal resolutions can lead to biased conclusions (Runge, Nowack, et al., 2019). Additionally, causal networks emphasize statistical relationships without directly diving into physical mechanisms, which may limit their interpretability and predictive power, especially in the context of changing climate conditions (Kretschmer et al., 2017). Furthermore, they struggle to capture nonlinear behaviors and threshold effects, which are critical in climate systems (Dijkstra, 2013; Runge, 2020). Consequently, while CENs provide insights, they need to be complemented with

19447973, 2024, 11, Downloaded from https://agupubs.onlinelibrary.wiley.com/doi/10.1029/2024WR038391 by Auburn University Libraries, Wiley Online Library on [24/02/2025]. See the Terms and Conditions (https://onlinelibrary.wiley.com/terms-and-conditions) on Wiley Online Library for rules of use; OA articles are governed by the applicable Creative Commons License

physical models, nonlinear dynamics, and multi-scale analyses to fully understand the complexities of hydroclimate systems.

The robustness of the CENs in identifying global drivers of FDs depends on the quality of meteorological and climate data. Our study uses the MERRA-2 data set, which benefits from the GEOS-5 model's advanced parameterizations, including gravity wave schemes for improved representation of tropical oscillations and additional assimilation of ground-based and satellite observations like Microwave Limb Sounder temperature data (Gong et al., 2022; Molod et al., 2015). However, limitations such as biases from model parameterizations, artificial damping (Rayleigh friction) at high altitudes, and uncertainties in assimilated observations could impact the validity of the causal inferences (Gong et al., 2022). Furthermore, runoff plays a significant role in the water budget; however, in this study, we did not include runoff for estimating WD due to the potentially large uncertainties associated with the global runoff reanalysis data, which would compromise the robustness of the results. Given the uncertainties from global reanalysis data, it deserves a separate study to incorporate runoff into WD estimation and FD analysis. Similarly, SMERGE SM data has notable limitations and uncertainties. Discontinuities in variance, likely due to changes in satellite instruments, observation systems, or land-use changes (Wang et al., 2021), can introduce artificial trends, complicating long-term analyses. The reanalysis data sets assimilated into SMERGE have evolved over time, causing inconsistencies between pre- and post-satellite periods, with degraded data quality in the 1980s and 1990s due to lower remote sensing frequency (Crow & Tobin, 2018). Additionally, interpolation of missing ESA-CCI data (Reichle et al., 2008) and RZSM measurement issues—such as coarse spatial and temporal resolutions, sampling biases, model uncertainties, and data assimilation errors—further contribute to uncertainties. These are common issues across similar data sets and do not significantly undermine the overall reliability of SMERGE. These points may affect the robustness of the causal relationships identified using the CEN method.

5. Conclusion

In summary, we identified local and remote regions that drive the occurrences of FDs using causal discovery analysis. Different regional and global processes can explain causal links from different parts of the world. Observed causal links suggest that FDs are driven by land–atmospheric interactions, Pacific/North Atlantic patterns, and the QBO, which affect SM. The Bermuda High influences FD events via changes in Z500. Large-scale processes like deep convection also influence them due to pressure differences, increased ET, and rising temperature due to global warming. We have also observed links from Indian, Atlantic, and Pacific Ocean regions suggesting that Global phenomena like IOD, ENSO, and MJO play a role through Rossby wave trains and jet streams. Moreover, atmospheric circulation forcings in South America could potentially affect the SAG FD through the low-level atmospheric flow, reducing inland moisture transport. In several study regions, regional scale processes like the Pacific Decadal Oscillation and California ARs influence SM. All discovered causal regions that are consistent with known teleconnection sources and potentially new sources are summarized in Table 2. Our research suggests that large-scale climate oscillations strongly influence FD through teleconnections, and these oscillations can serve as windows of opportunity for S2S forecasting. Finally, considering the regions with a direct connection from T2m, Z500, and WD influencing FD-pc in individual river basins, we successfully built a ML model to predict the FD events up to 4 weeks in advance. This accurate predictability also verifies our causal links and teleconnections from different parts of the world to US FD occurrences.

The findings from this work could lead to better understanding of the causality for extreme events in Earth systems and inform climate risk management and adaptation through improved early warning of FD by incorporating data-driven models, such as random forests demonstrated in this research. These models can improve predictive accuracy and extend forecast lead times by integrating the identified teleconnections. Tailored monitoring of key variables like WD, Z500 and T2m over identified regions, along with region-specific models, can provide proactive warnings for FD risks. Specific applications include their integration into established drought early warning systems such as the National Integrated Drought Information System, the United Nations Convention to Combat Desertification's (UNCCD) drought monitoring and forecasting system, Famine Early Warning Systems Network (FEWS NET), and Food and Agriculture Organization's drought system, which can enhance preparedness and regional forecasting of FD risks. Moreover, with the model's robustness and global teleconnections observed for FDs in three U.S. regions having distinct SM and climate patterns, we can conclude that the model can be re-run to other global hotspots of FDs to identify teleconnections affecting FDs at specific

locations. While the findings provide a solid foundation, regional variations in SM, land use, and climate patterns would need to be considered for broader global applicability.

Conflict of Interest

The authors declare no conflicts of interest relevant to this study.

Data Availability Statement

All the data used in this research are publicly available. The SMERG RZSM data were obtained from the Goddard Earth Sciences Data and Information Services Center (Crow & Tobin, 2018). Other hydroclimate data sets from MERRA2 were obtained from the GMAO (GMAO, 2015a, 2015b, 2015c). The data and computer scripts generated from this study is shared publicly at the Open Science Framework (Kumar & Tian, 2024).

Acknowledgments
This work is supported by the NSF CAREER Award (EAR-2144293). We would like to thank high-performance computing support provided by the National Center of Atmospheric Research. We also thank Hailan Wang from NOAA Climate Prediction Center for useful discussions at the early stage of this work. We also thank the three anonymous reviewers for their valuable comments, which improved the quality of the research paper.

References

Ambrizzi, T., Hoskins, B. J., & Hsu, H. H. (1995). Rossby wave propagation and teleconnection patterns in the austral winter. *Journal of the Atmospheric Sciences*, *52*(21), 3661–3672. https://doi.org/10.1175/1520-0469(1995)052<3661:rwpatp>2.0.co;2

Arcodia, M. C., Kirtman, B. P., & Siqueira, L. S. (2020). How MJO teleconnections and ENSO interference impacts US precipitation. *Journal of Climate*, *33*(11), 4621–4640. https://doi.org/10.1175/jcli-d-19-0448.1

Beaudin, É., Di Lorenzo, E., Miller, A. J., Seo, H., & Joh, Y. (2023). Impact of extratropical Northeast Pacific SST on US West Coast precipitation. *Geophysical Research Letters*, *50*(3), e2022GL102354. https://doi.org/10.1029/2022gl102354

Bosilovich, M. G., Lucchesi, R., & Suarez, M. (2015). MERRA-2: File specification GMAO Office Note No. 9 (Version 1.0) [Dataset], 73. http://gmao.gsfc.nasa.gov/pubs/office_notes

Breiman, L. (2001). Random forests. *Machine Learning*, *45*(1), 5–32. https://doi.org/10.1023/a:1010933404324

Chawla, N. V., Bowyer, K. W., Hall, L. O., & Kegelmeyer, W. P. (2002). SMOTE: Synthetic minority over-sampling technique. *Journal of Artificial Intelligence Research*, *16*, 321–357. https://doi.org/10.1613/jair.953

Chiang, F., Mazdiyasni, O., & AghaKouchak, A. (2021). Evidence of anthropogenic impacts on global drought frequency, duration, and intensity. *Nature Communications*, *12*(1), 1–10. https://doi.org/10.1038/s41467-021-22314-w

Christian, J. I., Basara, J. B., Hunt, E. D., Otkin, J. A., & Xiao, X. (2020). Flash drought development and cascading impacts associated with the 2010 Russian heatwave. *Environmental Research Letters*, *15*(9), 094078. https://doi.org/10.1088/1748-9326/ab9faf

Clark, J. P., & Feldstein, S. B. (2022). The temperature anomaly pattern of the Pacific–North American teleconnection: Growth and decay. *Journal of the Atmospheric Sciences*, *79*(5), 1237–1252. https://doi.org/10.1175/jas-d-21-0030.1

Corak, N. K., Otkin, J. A., Ford, T. W., & Lowman, L. E. (2024). Unraveling phenological and stomatal responses to flash drought and implications for water and carbon budgets. *Hydrology and Earth System Sciences*, *28*(8), 1827–1851. https://doi.org/10.5194/hess-28-1827-2024

Crow, W., & Tobin, K. (2018). Smerge-Noah-CCI root zone soil moisture 0-40 cm L4 daily 0.125 x 0.125 degree V2.0, Greenbelt, Maryland, USA Goddard Earth Sciences Data and Information Services Center (GES DISC), [Dataset]. https://doi.org/10.5067/PAVQY1KHTMUT

Dangendorf, S., Rybski, D., Mudersbach, C., Müller, A., Kaufmann, E., Zorita, E., & Jensen, J. (2014). Evidence for long-term memory in sea level. *Geophysical Research Letters*, *41*(15), 5530–5537. https://doi.org/10.1002/2014gl060538

Davis, J., & Goadrich, M. (2006). The relationship between Precision-Recall and ROC curves. In *Proceedings of the 23rd international conference on Machine learning* (pp. 233–240).

DeAngelis, A. M., Wang, H., Koster, R. D., Schubert, S. D., Chang, Y., & Marshak, J. (2020). Prediction skill of the 2012 US Great Plains flash drought in Subseasonal Experiment (SubX) models. *Journal of Climate*, *33*(14), 6229–6253. https://doi.org/10.1175/jcli-d-19-0863.1

de Moraes, F. A., Moreira, S. G., Peixoto, D. S., Silva, J. C. R., Macedo, J. R., Silva, M. M., et al. (2023). Lime incorporation up to 40 cm deep increases root growth and crop yield in highly weathered tropical soils. *European Journal of Agronomy*, *144*, 126763. https://doi.org/10.1016/j.eja.2023.126763

Deng, S., Tan, X., Liu, B., Yang, F., & Yan, T. (2022). A reversal in global occurrences of flash drought around 2000 identified by rapid changes in the standardized evaporative stress ratio. *Science of the Total Environment*, *848*, 157427. https://doi.org/10.1016/j.scitotenv.2022.157427

Dettinger, M. D. (2013). Atmospheric rivers as drought busters on the US West Coast. *Journal of Hydrometeorology*, *14*(6), 1721–1732. https://doi.org/10.1175/jhm-d-13-02.1

Di Capua, G., Runge, J., Donner, R. V., van den Hurk, B., Turner, A. G., Vellore, R., et al. (2020). Dominant patterns of interaction between the tropics and mid-latitudes in boreal summer: Causal relationships and the role of timescales. *Weather and Climate Dynamics*, *1*(2), 519–539. https://doi.org/10.5194/wcd-1-519-2020

Dijkstra, H. A. (2013). *Nonlinear climate dynamics*. Cambridge University Press.

Donges, J. F., Zou, Y., Marwan, N., & Kurths, J. (2009). Complex networks in climate dynamics: Comparing linear and nonlinear network construction methods. *The European Physical Journal Special Topics*, *174*(1), 157–179. https://doi.org/10.1140/epjst/e2009-01098-2

Ester, M., Kriegel, H. P., Sander, J., & Xu, X. (1996). A density-based algorithm for discovering clusters in large spatial databases with noise. *kdd*, *96*(34), 226–231.

Fan, J., McConkey, B., Wang, H., & Janzen, H. (2016). Root distribution by depth for temperate agricultural crops. *Field Crops Research*, *189*, 68–74. https://doi.org/10.1016/j.fcr.2016.02.013

Fernández, A., Garcia, S., Herrera, F., & Chawla, N. V. (2018). SMOTE for learning from imbalanced data: Progress and challenges, marking the 15-year anniversary. *Journal of Artificial Intelligence Research*, *61*, 863–905. https://doi.org/10.1613/jair.1.11192

Ford, T. W., & Labosier, C. F. (2017). Meteorological conditions associated with the onset of flash drought in the eastern United States. *Agricultural and Forest Meteorology*, *247*, 414–423. https://doi.org/10.1016/j.agrformet.2017.08.031

Gelaro, R., McCarty, W., Suárez, M. J., Todling, R., Molod, A., Takacs, L., et al. (2017). The modern-era retrospective analysis for research and applications, version 2 (MERRA-2). *Journal of Climate*, *30*(14), 5419–5454. https://doi.org/10.1175/jcli-d-16-0758.1

19447973, 2024, 11, Downloaded from https://agupubs.onlinelibrary.wiley.com/doi/10.1029/2024WR038391 by Auburn University Libraries, Wiley Online Library on [24/02/2025]. See the Terms and Conditions (https://onlinelibrary.wiley.com/terms-and-conditions) on Wiley Online Library for rules of use; OA articles are governed by the applicable Creative Commons License

GMAO. (2015a). MERRA-2 inst6_3d_ana_Np: 3d, 6-hourly, instantaneous, pressure-level, analysis, analyzed meteorological fields V5.12.4, Greenbelt, MD, USA Goddard Earth Sciences Data and Information Services Center (GES DISC), [Dataset]. https://doi.org/10.5067/A7S6XP56VZWS

GMAO. (2015b). MERRA-2 tavg1_2d_flx_Nx: 2d, 1-hourly, time-averaged, single-level, assimilation, surface flux diagnostics V5.12.4, Greenbelt, MD, USA Goddard Earth Sciences Data and Information Services Center (GES DISC), [Dataset]. https://doi.org/10.5067/7MCPBJ41Y0K6

GMAO. (2015c). MERRA-2 tavg1_2d_slv_Nx: 2d, 1-hourly, time-averaged, single-level, assimilation, single-level diagnostics V5.12.4, Greenbelt, MD, USA Goddard Earth Sciences Data and Information Services Center (GES DISC), [Dataset]. https://doi.org/10.5067/VJAFPLI1CSIV

Gong, Y., Yang, S., Yin, J., Wang, S., Pan, X., Li, D., & Yi, X. (2022). Validation of the reproducibility of warm-season northeast China cold vortices for ERA5 and MERRA-2 reanalysis. *Journal of Applied Meteorology and Climatology*, *61*(9), 1349–1366. https://doi.org/10.1175/jamc-d-22-0052.1

Goswami, B. N., Chakraborty, D., Rajesh, P. V., & Mitra, A. (2022). Predictability of South-Asian monsoon rainfall beyond the legacy of Tropical Ocean Global Atmosphere program (TOGA). *npj Climate and Atmospheric Science*, *5*(1), 58. https://doi.org/10.1038/s41612-022-00281-3

Granger, C. W. (1969). Investigating causal relations by econometric models and cross-spectral methods. *Econometrica: Journal of the Econometric Society*, *37*(3), 424–438. https://doi.org/10.2307/1912791

Gray, S. L., Dunning, C. M., Methven, J., Masato, G., & Chagnon, J. M. (2014). Systematic model forecast error in Rossby wave structure. *Geophysical Research Letters*, *41*(8), 2979–2987. https://doi.org/10.1002/2014gl059282

Hansen, J. W., Hodges, A. W., & Jones, J. W. (1998). ENSO influences on agriculture in the southeastern United States. *Journal of Climate*, *11*(3), 404–411. https://doi.org/10.1175/1520-0442(1998)011<0404:eioait>2.0.co;2

He, H., & Garcia, E. A. (2009). Learning from imbalanced data. *IEEE Transactions on Knowledge and Data Engineering*, *21*(9), 1263–1284. https://doi.org/10.1109/tkde.2008.239

Hoell, A., Parker, B. A., Downey, M., Umphlett, N., Jencso, K., Akyuz, F. A., et al. (2020). Lessons learned from the 2017 flash drought across the US Northern Great Plains and Canadian Prairies. *Bulletin of the American Meteorological Society*, *101*(12), 1–46. https://doi.org/10.1175/bams-d-19-0272.1

Hoerling, M., Eischeid, J., Kumar, A., Leung, R., Mariotti, A., Mo, K., et al. (2014). Causes and predictability of the 2012 Great Plains drought. *Bulletin of the American Meteorological Society*, *95*(2), 269–282. https://doi.org/10.1175/bams-d-13-00055.1

Hoffmann, D., Gallant, A. J., & Hobbins, M. (2021). Flash drought in CMIP5 models. *Journal of Hydrometeorology*, *22*(6), 1439–1454. https://doi.org/10.1175/jhm-d-20-0262.1

Hung, F., Son, K., & Yang, Y. E. (2022). Investigating uncertainties in human adaptation and their impacts on water scarcity in the Colorado river Basin, United States. *Journal of Hydrology*, *612*, 128015. https://doi.org/10.1016/j.jhydrol.2022.128015

Konapala, G., & Mishra, A. (2017). Review of complex networks application in hydroclimatic extremes with an implementation to characterize spatio-temporal drought propagation in continental USA. *Journal of Hydrology*, *555*, 600–620. https://doi.org/10.1016/j.jhydrol.2017.10.033

Koster, R. D., Schubert, S. D., Wang, H., Mahanama, S. P., & DeAngelis, A. M. (2019). Flash drought as captured by reanalysis data: Disentangling the contributions of precipitation deficit and excess evapotranspiration. *Journal of Hydrometeorology*, *20*(6), 1241–1258. https://doi.org/10.1175/jhm-d-18-0242.1

Kretschmer, M., Cohen, J., Matthias, V., Runge, J., & Coumou, D. (2018). The different stratospheric influence on cold-extremes in Eurasia and North America. *npj Climate and Atmospheric Science*, *1*(1), 44. https://doi.org/10.1038/s41612-018-0054-4

Kretschmer, M., Coumou, D., Donges, J. F., & Runge, J. (2016). Using causal effect networks to analyze different Arctic drivers of midlatitude winter circulation. *Journal of Climate*, *29*(11), 4069–4081. https://doi.org/10.1175/jcli-d-15-0654.1

Kretschmer, M., Runge, J., & Coumou, D. (2017). Early prediction of extreme stratospheric polar vortex states based on causal precursors. *Geophysical Research Letters*, *44*(16), 8592–8600. https://doi.org/10.1002/2017gl074696

Kumar, R., Kuttippurath, J., Gopikrishnan, G. S., Kumar, P., & Varikoden, H. (2023). Enhanced surface temperature over India during 1980–2020 and future projections: Causal links of the drivers and trends. *npj Climate and Atmospheric Science*, *6*(1), 164. https://doi.org/10.1038/s41612-023-00494-0

Kumar, S., & Tian, D. (2024). Causal discovery analysis reveals global sources of predictability for regional flash droughts [Dataset]. OSF. https://doi.org/10.17605/OSF.IO/C9YGJ

Lehmann, J., Kretschmer, M., Schauberger, B., & Wechsung, F. (2020). Potential for early forecast of Moroccan wheat yields based on climatic drivers. *Geophysical Research Letters*, *47*(12), e2020GL087516. https://doi.org/10.1029/2020gl087516

Lesinger, K., & Tian, D. (2022). Trends, variability, and drivers of flash droughts in the contiguous United States. *Water Resources Research*, *58*(9), e2022WR032186. https://doi.org/10.1029/2022wr032186

Lesinger, K., Tian, D., & Wang, H. (2024). Subseasonal forecast skill of evaporative demand, soil moisture, and flash drought onset from two dynamic models over the contiguous United States. *Journal of Hydrometeorology*, *25*(7), 965–990. https://doi.org/10.1175/JHM-D-23-0124.1

Li, R., Chen, N., Zhang, X., Zeng, L., Wang, X., Tang, S., et al. (2020). Quantitative analysis of agricultural drought propagation process in the Yangtze River Basin by using cross wavelet analysis and spatial autocorrelation. *Agricultural and Forest Meteorology*, *280*, 107809. https://doi.org/10.1016/j.agrformet.2019.107809

Lim, Y. K. (2015). The East Atlantic/West Russia (EA/WR) teleconnection in the North Atlantic: Climate impact and relation to Rossby wave propagation. *Climate Dynamics*, *44*(11–12), 3211–3222. https://doi.org/10.1007/s00382-014-2381-4

Lisonbee, J., Woloszyn, M., & Skumanich, M. (2022). Making sense of flash drought: Definitions, indicators, and where we go from here. *Journal of Applied and Service Climatology*, *2021*(001), 1–19. https://doi.org/10.46275/joasc.2021.02.001

Liu, E., Zhu, Y., Lü, H., Horton, R., Gou, Q., Wang, X., et al. (2023). Estimation and assessment of the root zone soil moisture from near-surface measurements over Huai River basin. *Atmosphere*, *14*(1), 124. https://doi.org/10.3390/atmos14010124

Lorenz, D. J., Otkin, J. A., Zaitchik, B., Hain, C., & Anderson, M. C. (2021). Predicting rapid changes in evaporative stress index (ESI) and soil moisture anomalies over the continental United States. *Journal of Hydrometeorology*, *22*(11), 3017–3036. https://doi.org/10.1175/jhm-d-20-0289.1

Luo, H., Adames, Á. F., & Rood, R. B. (2021). A northern hemispheric wave train associated with interannual variations in the Bermuda high during boreal summer. *Journal of Climate*, *34*(15), 6163–6173. https://doi.org/10.1175/jcli-d-20-0608.1

Ma, R., & Yuan, X. (2023). Subseasonal ensemble prediction of flash droughts over China. *Journal of Hydrometeorology*, *24*(5), 897–910. https://doi.org/10.1175/jhm-d-22-0150.1

Mahto, S. S., & Mishra, V. (2023). Increasing risk of simultaneous occurrence of flash drought in major global croplands. *Environmental Research Letters*, *18*(4), 044044. https://doi.org/10.1088/1748-9326/acc8ed

19447973, 2024, 11, Downloaded from https://agupubs.onlinelibrary.wiley.com/doi/10.1029/2024WR038391 by Auburn University Libraries, Wiley Online Library on [24/02/2025]. See the Terms and Conditions (https://onlinelibrary.wiley.com/terms-and-conditions) on Wiley Online Library for rules of use; OA articles are governed by the applicable Creative Commons License

Malloy, K., & Kirtman, B. P. (2023). Subseasonal great plains rainfall via remote extratropical teleconnections: Regional application of theory-Guided causal networks. *Journal of Geophysical Research: Atmospheres*, *128*(5), e2022JD037795. https://doi.org/10.1029/2022jd037795

Manthos, Z. H., Pegion, K. V., Dirmeyer, P. A., & Stan, C. (2022). The relationship between surface weather over North America and the Mid-Latitude Seasonal Oscillation. *Dynamics of Atmospheres and Oceans*, *99*, 101314. https://doi.org/10.1016/j.dynatmoce.2022.101314

McIntosh, P. C., & Hendon, H. H. (2018). Understanding Rossby wave trains forced by the Indian Ocean Dipole. *Climate Dynamics*, *50*(7–8), 2783–2798. https://doi.org/10.1007/s00382-017-3771-1

McKinnon, K. A., Rhines, A., Tingley, M. P., & Huybers, P. (2016). Long-lead predictions of eastern United States hot days from Pacific sea surface temperatures. *Nature Geoscience*, *9*(5), 389–394. https://doi.org/10.1038/ngeo2687

Miralles, D. G., Gentine, P., Seneviratne, S. I., & Teuling, A. J. (2019). Land–atmospheric feedbacks during droughts and heatwaves: State of the science and current challenges. *Annals of the New York Academy of Sciences*, *1436*(1), 19–35. https://doi.org/10.1111/nyas.13912

Mishra, A., Vu, T., Veettil, A. V., & Entekhabi, D. (2017). Drought monitoring with soil moisture active passive (SMAP) measurements. *Journal of Hydrology*, *552*, 620–632. https://doi.org/10.1016/j.jhydrol.2017.07.033

Mishra, A. K., & Singh, V. P. (2010). A review of drought concepts. *Journal of Hydrology*, *391*(1–2), 202–216. https://doi.org/10.1016/j.jhydrol.2010.07.012

Mo, K. C., & Lettenmaier, D. P. (2015). Heat wave flash droughts in decline. *Geophysical Research Letters*, *42*(8), 2823–2829. https://doi.org/10.1002/2015gl064018

Mo, K. C., & Lettenmaier, D. P. (2016). Precipitation deficit flash droughts over the United States. *Journal of Hydrometeorology*, *17*(4), 1169–1184. https://doi.org/10.1175/jhm-d-15-0158.1

Mo, K. C., & Lettenmaier, D. P. (2020). Prediction of flash droughts over the United States. *Journal of Hydrometeorology*, *21*(8), 1793–1810. https://doi.org/10.1175/jhm-d-19-0221.1

Molod, A., Takacs, L., Suarez, M., & Bacmeister, J. (2015). Development of the GEOS-5 atmospheric general circulation model: Evolution from MERRA to MERRA2. *Geoscientific Model Development*, *8*(5), 1339–1356. https://doi.org/10.5194/gmd-8-1339-2015

Novick, K. A., Ficklin, D. L., Stoy, P. C., Williams, C. A., Bohrer, G., Oishi, A. C., et al. (2016). The increasing importance of atmospheric demand for ecosystem water and carbon fluxes. *Nature Climate Change*, *6*(11), 1023–1027. https://doi.org/10.1038/nclimate3114

Nowack, P., Runge, J., Eyring, V., & Haigh, J. D. (2020). Causal networks for climate model evaluation and constrained projections. *Nature Communications*, *11*(1), 1415. https://doi.org/10.1038/s41467-020-15195-y

Osman, M., Zaitchik, B. F., Badr, H. S., Christian, J. I., Tadesse, T., Otkin, J. A., & Anderson, M. C. (2021). Flash drought onset over the contiguous United States: Sensitivity of inventories and trends to quantitative definitions. *Hydrology and Earth System Sciences*, *25*(2), 565–581. https://doi.org/10.5194/hess-25-565-2021

Osman, M., Zaitchik, B. F., Badr, H. S., Otkin, J., Zhong, Y., Lorenz, D., et al. (2022). Diagnostic classification of flash drought events reveals distinct classes of forcings and impacts. *Journal of Hydrometeorology*, *23*(2), 275–289. https://doi.org/10.1175/jhm-d-21-0134.1

Otkin, J. A., Anderson, M. C., Hain, C., Mladenova, I. E., Basara, J. B., & Svoboda, M. (2013). Examining rapid onset drought development using the thermal infrared–based evaporative stress index. *Journal of Hydrometeorology*, *14*(4), 1057–1074. https://doi.org/10.1175/jhm-d-12-0144.1

Otkin, J. A., Zhong, Y., Hunt, E. D., Basara, J., Svoboda, M., Anderson, M. C., & Hain, C. (2019). Assessing the evolution of soil moisture and vegetation conditions during a flash drought–flash recovery sequence over the South-Central United States. *Journal of Hydrometeorology*, *20*(3), 549–562. https://doi.org/10.1175/jhm-d-18-0171.1

Pendergrass, A. G., Meehl, G. A., Pulwarty, R., Hobbins, M., Hoell, A., AghaKouchak, A., et al. (2020). Flash droughts present a new challenge for subseasonal-to-seasonal prediction. *Nature Climate Change*, *10*(3), 191–199. https://doi.org/10.1038/s41558-020-0709-0

Ralph, F. M., & Dettinger, M. D. (2011). Storms, floods, and the science of atmospheric rivers. *Eos, Transactions American Geophysical Union*, *92*(32), 265–266. https://doi.org/10.1029/2011eo320001

Reichle, R. H., Crow, W. T., Koster, R. D., Sharif, H. O., & Mahanama, S. P. P. (2008). Contribution of soil moisture retrievals to land data assimilation products. *Geophysical Research Letters*, *35*(1). https://doi.org/10.1029/2007gl031986

Ren, X., Liu, W., Capotondi, A., Amaya, D. J., & Holbrook, N. J. (2023). The Pacific Decadal Oscillation modulated marine heatwaves in the Northeast Pacific during past decades. *Communications Earth & Environment*, *4*(1), 218. https://doi.org/10.1038/s43247-023-00863-w

Rigden, A. J., Mueller, N. V., Holbrook, N. M., Pillai, N., & Huybers, P. (2020). Combined influence of soil moisture and atmospheric evaporative demand is important for accurately predicting US maize yields. *Nature Food*, *1*(2), 127–133. https://doi.org/10.1038/s43016-020-0028-7

Roy, T., Martinez, J. A., Herrera-Estrada, J. E., Zhang, Y., Dominguez, F., Berg, A., et al. (2019). Role of moisture transport and recycling in characterizing droughts: Perspectives from two recent US droughts and the CFSv2 system. *Journal of Hydrometeorology*, *20*(1), 139–154. https://doi.org/10.1175/jhm-d-18-0159.1

Runge, J. (2020). Discovering contemporaneous and lagged causal relations in autocorrelated nonlinear time series datasets. In *Conference on uncertainty in Artificial Intelligence* (pp. 1388–1397). Pmlr.

Runge, J., Bathiany, S., Bollt, E., Camps-Valls, G., Coumou, D., Deyle, E., et al. (2019). Inferring causation from time series in Earth system sciences. *Nature Communications*, *10*(1), 1–13. https://doi.org/10.1038/s41467-019-10105-3

Runge, J., Nowack, P., Kretschmer, M., Flaxman, S., & Sejdinovic, D. (2019). Detecting and quantifying causal associations in large nonlinear time series datasets. *Science Advances*, *5*(11), eaau4996. https://doi.org/10.1126/sciadv.aau4996

Saito, T., & Rehmsmeier, M. (2015). The precision-recall plot is more informative than the ROC plot when evaluating binary classifiers on imbalanced datasets. *PLoS One*, *10*(3), 233–240. https://doi.org/10.1371/journal.pone.0118432

Schubert, S., Wang, H., & Suarez, M. (2011). Warm season subseasonal variability and climate extremes in the Northern Hemisphere: The role of stationary Rossby waves. *Journal of Climate*, *24*(18), 4773–4792. https://doi.org/10.1175/jcli-d-10-05035.1

Schubert, S. D., Chang, Y., DeAngelis, A. M., Wang, H., & Koster, R. D. (2021). On the development and demise of the Fall 2019 southeast US flash drought: Links to an extreme positive IOD. *Journal of Climate*, *34*(5), 1701–1723. https://doi.org/10.1175/jcli-d-20-0428.1

Sellars, S. L., Kawzenuk, B., Nguyen, P., Ralph, F. M., & Sorooshian, S. (2017). Genesis, pathways, and terminations of intense global water vapor transport in association with large-scale climate patterns. *Geophysical Research Letters*, *44*(24), 12–465. https://doi.org/10.1002/2017gl075495

Seneviratne, S. I., Nicholls, N., Easterling, D., Goodess, C., Kanae, S., Kossin, J., et al. (2012). Managing the risks of extreme events and disasters to advance climate change adaptation. In *A special report of working groups I and II of the Intergovernmental Panel on Climate Change (IPCC)* (pp. 109–230). Changes in climate extremes and their impacts on the natural physical environment.

Shin, C. S., Dirmeyer, P. A., & Huang, B. (2023). A joint approach combining correlation and mutual information to study land and ocean drivers of us droughts: Methodology. *Journal of Climate*, *36*(9), 2795–2814. https://doi.org/10.1175/jcli-d-22-0429.1

Spirtes, P., & Glymour, C. (1991). An algorithm for fast recovery of sparse causal graphs. *Social Science Computer Review*, *9*(1), 62–72. https://doi.org/10.1177/089443939100900106

19447973, 2024, 11, Downloaded from https://agupubs.onlinelibrary.wiley.com/doi/10.1029/2024WR038391 by Auburn University Libraries, Wiley Online Library on [24/02/2025]. See the Terms and Conditions (https://onlinelibrary.wiley.com/terms-and-conditions) on Wiley Online Library for rules of use; OA articles are governed by the applicable Creative Commons License

Su, L., Cao, Q., Shukla, S., Pan, M., & Lettenmaier, D. P. (2023). Evaluation of subseasonal drought forecast skill over the coastal western United States. *Journal of Hydrometeorology*, *24*(4), 709–726. https://doi.org/10.1175/jhm-d-22-0103.1

Svoboda, M., LeComte, D., Hayes, M., Heim, R., Gleason, K., Angel, J., et al. (2002). The drought monitor. *Bulletin of the American Meteorological Society*, *83*(8), 1181–1190. https://doi.org/10.1175/1520-0477-83.8.1181

Teuling, A. J., Van Loon, A. F., Seneviratne, S. I., Lehner, I., Aubinet, M., Heinesch, B., et al. (2013). Evapotranspiration amplifies European summer drought. *Geophysical Research Letters*, *40*(10), 2071–2075. https://doi.org/10.1002/grl.50495

Tian, D., Pan, M., Jia, L., Vincci, G., & Wood, E. F. (2016). Assessing GFDL high-resolution climate model water and energy budgets from AMIP simulations over Africa. *Journal of Geophysical Research-Atmosphere*, *121*(14), 8444–8459. https://doi.org/10.1002/2016jd025068

Tian, D., Pan, M., & Wood, E. F. (2018). Assessment of a high-resolution climate model for surface water and energy flux simulations over global land: An inter-comparison with reanalyses. *Journal of Hydrometeorology*, *19*(7), 1115–1129. https://doi.org/10.1175/jhm-d-17-0156.1

Tobin, K. J., Crow, W. T., & Bennett, M. E. (2021). Root zone soil moisture comparisons: AirMOSS, SMERGE, and SMAP. *IEEE Geoscience and Remote Sensing Letters*, *19*, 1–5. https://doi.org/10.1109/lgrs.2021.3085432

Tobin, K. J., Crow, W. T., Dong, J., & Bennett, M. E. (2019). Validation of a new root-zone soil moisture product: Soil MERGE. *IEEE Journal of Selected Topics in Applied Earth Observations and Remote Sensing*, *12*(9), 3351–3365. https://doi.org/10.1109/jstars.2019.2930946

Tran, H., Zhang, J., O'Neill, M. M., Ryken, A., Condon, L. E., & Maxwell, R. M. (2022). A hydrological simulation dataset of the Upper Colorado River Basin from 1983 to 2019. *Scientific Data*, *9*(1), 16. https://doi.org/10.1038/s41597-022-01123-w

Tyagi, S., Zhang, X., Saraswat, D., Sahany, S., Mishra, S. K., & Niyogi, D. (2022). Flash drought: Review of concept, prediction and the potential for machine learning, deep learning methods. *Earth's Future*, *10*(11), e2022EF002723. https://doi.org/10.1029/2022ef002723

USDA National Agricultural Statistics Service, 2017 Census of Agriculture. [Dataset]. www.nass.usda.gov/AgCensus

USDA National Agricultural Statistics Service Cropland Data Layer. (2014). Published crop-specific data layer [online]. USDA-NASS, Washington, DC.

Vijverberg, S., & Coumou, D. (2022). The role of the Pacific Decadal Oscillation and ocean-atmosphere interactions in driving US temperature predictability. *npj Climate and Atmospheric Science*, *5*(1), 18. https://doi.org/10.1038/s41612-022-00237-7

Wang, H., Schubert, S., Koster, R., Ham, Y. G., & Suarez, M. (2014). On the role of SST forcing in the 2011 and 2012 extreme US heat and drought: A study in contrasts. *Journal of Hydrometeorology*, *15*(3), 1255–1273. https://doi.org/10.1175/jhm-d-13-069.1

Wang, S., Ma, X., Zhou, S., Wu, L., Wang, H., Tang, Z., et al. (2023). Extreme atmospheric rivers in a warming climate. *Nature Communications*, *14*(1), 3219. https://doi.org/10.1038/s41467-023-38980-x

Wang, Y., Mao, J., Jin, M., Hoffman, F. M., Shi, X., Wullschleger, S. D., & Dai, Y. (2021). Development of observation-based global multilayer soil moisture products for 1970 to 2016. *Earth System Science Data*, *13*(9), 4385–4405. https://doi.org/10.5194/essd-13-4385-2021

Wang, Y., & Yuan, X. (2022). Land-atmosphere coupling speeds up flash drought onset. *Science of the Total Environment*, *851*, 158109. https://doi.org/10.1016/j.scitotenv.2022.158109

Yin, X., Wu, Y., Zhao, W., Liu, S., Zhao, F., Chen, J., et al. (2023). Spatiotemporal responses of net primary productivity of alpine ecosystems to flash drought: The Qilian Mountains. *Journal of Hydrology*, *624*, 129865. https://doi.org/10.1016/j.jhydrol.2023.129865

Yuan, X., Wang, L., Wu, P., Ji, P., Sheffield, J., & Zhang, M. (2019). Anthropogenic shift towards higher risk of flash drought over China. *Nature Communications*, *10*(1), 4661. https://doi.org/10.1038/s41467-019-12692-7

Yuan, X., Wang, Y., Ji, P., Wu, P., Sheffield, J., & Otkin, J. A. (2023). A global transition to flash droughts under climate change. *Science*, *380*(6641), 187–191. https://doi.org/10.1126/science.abn6301

Zhang, J., Yang, Z., Wu, L., & Yang, K. (2019). Summer high temperature extremes over Northeastern China predicted by spring soil moisture. *Scientific Reports*, *9*(1), 12577. https://doi.org/10.1038/s41598-019-49053-9

Zhang, X., Chen, N., Li, J., Chen, Z., & Niyogi, D. (2017). Multi-sensor integrated framework and index for agricultural drought monitoring. *Remote Sensing of Environment*, *188*, 141–163. https://doi.org/10.1016/j.rse.2016.10.045

Zhou, H., Zhou, W., Liu, Y., Yuan, Y., Huang, J., & Liu, Y. (2020). Identifying spatial extent of meteorological droughts: An examination over a humid region. *Journal of Hydrology*, *591*, 125505. https://doi.org/10.1016/j.jhydrol.2020.125505

19447973, 2024, 11, Downloaded from https://agupubs.onlinelibrary.wiley.com/doi/10.1029/2024WR038391 by Auburn University Libraries, Wiley Online Library on [24/02/2025]. See the Terms and Conditions (https://onlinelibrary.wiley.com/terms-and-conditions) on Wiley Online Library for rules of use; OA articles are governed by the applicable Creative Commons License